CHEMISTRY OF
MATERIALS
Review

Chem. Mater. **2010,** *22,* 691–714 691
DOI:10.1021/cm902696j

Positive Electrode Materials for Li-Ion and Li-Batteries[†]

Brian L. Ellis, Kyu Tae Lee, and Linda F. Nazar*

University of Waterloo, Department of Chemistry, Waterloo, Ontario, Canada N2L 3G1

Received August 31, 2009. Revised Manuscript Received November 23, 2009

Positive electrodes for Li-ion and lithium batteries (also termed “cathodes”) have been under intense scrutiny since the advent of the Li-ion cell in 1991. This is especially true in the past decade. Early on, carbonaceous materials dominated the negative electrode and hence most of the possible improvements in the cell were anticipated at the positive terminal; on the other hand, major developments in negative electrode materials made in the last portion of the decade with the introduction of nanocomposite Sn/C/Co alloys and Si−C composites have demanded higher capacity positive electrodes to match. Much of this was driven by the consumer market for small portable electronic devices. More recently, there has been a growing interest in developing Li−sulfur and Li−air batteries that have the potential for vastly increased capacity and energy density, which is needed to power large-scale systems. These require even more complex assemblies at the positive electrode in order to achieve good properties. This review provides an overview of the major developments in the area of positive electrode materials in both Li-ion and Li batteries in the past decade, and particularly in the past few years. Highlighted are concepts in solid-state chemistry and nanostructured materials that conceptually have provided new opportunities for materials scientists for tailored design that can be extended to many different electrode materials.

1. Introduction

The demands for advanced energy storage devices have increased significantly each year for the past decade. They are motivated by a variety of different needs, but all have in common the potential benefits for our technologically driven, highly mobile, energy challenged society. Efforts in the recent past have been primarily spurred by portable and miniaturized electronics, aerospace and military applications, uninterrupted power supplies for technological and rural needs, power tools, and other transportable devices. Although these will still remain far into the future, more pressing needs will be driven by the efficient use of renewable energies where energy storage provides critical load leveling, and for electric vehicles to mitigate petroleum consumption and urban pollution. The requirements of the appropriate energy storage device differ notably in each area. Hence research in the field of rechargeable batteries has intensified in the past decade to attempt to meet these demands.

The earliest configuration of rechargeable lithium cells used metallic lithium or Li−Al alloys as the negative electrode, with a variety of chalcogenides (TiS_2, MoS_2, etc.),[1] as the positive electrode in several prototypes and commercial products. Later, manganese and vanadium oxides were utilized. Lithium metal as an anode material in rechargeable batteries was ultimately rejected due to safety concerns, owing to dendrite growth on the metal surface after repeated Li plating that led to internal short circuits. Following the discovery of $LiCoO_2$ as a positive electrode, the commercialization of the Li-ion battery by SONY provided a step change in the approach to energy storage.[2] They combined $LiCoO_2$ with negative electrodes comprised of carbonaceous materials which provided a host for Li^+ ions at low potential, thus removing metallic lithium from the cell. Their domination in the market thus meant that much of the subsequent improvements in the cell were focused on developing new positive terminal materials or “cathode”. But more recently, the introduction of nanocomposites comprised of Sn/C/Co alloys or Si−C led to major developments in negative electrode materials during the last portion of the decade. They require higher capacity positive electrodes to provide optimum utilization of the storage properties.

Layered lithium transition metal oxides arguably represent the most successful category of positive electrode, comprising compounds with formula of $LiMO_2$ (M: Mn, Co, and Ni) that crystallize in a layered structure. This topology offers highly accessible ion diffusion pathways. However, considerable interest in a new class of transition metal phosphate materials was sparked by the introduction of $LiFePO_4$ as a cathode material about 10 years ago. More than a thousand papers on this topic have been published since then, the research being motivated by many factors. Much more recently, there is a growing interest in developing Li−sulfur and Li−air batteries, which have the potential for vastly increased capacity and energy density that could reach levels needed in large-scale power systems. These require even more complex assemblies at the positive electrode. Currently,

---

[†] Accepted as part of the 2010 “Materials Chemistry of Energy Conversion Special Issue”.

*Corresponding author. E-mail: lfnazar@uwaterloo.ca.

they have invoked a return to (protected) metallic lithium negative electrodes, although future progress will likely take place with new electrolytes and high capacity nonmetallic anodes.

This review provides an overview of selected developments in the area of positive electrode materials in both Li-ion and Li batteries in the past decade, and particularly in the past few years. To cover all of the immense body of work published in this time period would be beyond the scope of the article. This article focuses on major developments in three areas − lithium metal phosphates; lithium metal oxides and intergrowth structures; and composite positive electrodes for Li−S and Li−air. Highlighted are concepts in solid-state chemistry and nanostructured materials that conceptually have provided materials scientists with new opportunities for tailored design that can be extended to many different electrode materials.

2. Polyanion-Based Positive Electrodes

Although transition metal oxides (discussed in subsequent sections) are commonly used as energy storage materials in today's modern portable devices, concerns over safety and cost have prompted research into other new electrode materials for lithium ion batteries. Several new compounds have been explored as possible alternatives, including those obtained by introducing large polyanions of the form $(XO_4)^{y-}$ (X = S, P, Si, As, Mo, W) into the lattice. An inductive effect from $(PO_4)^{3-}$ and $(SO_4)^{2-}$ ions raises redox energies compared to those in oxides and stabilizes the structure.[3] The presence of the polyanion $(XO_4)^{y-}$ with strong X−O covalent bonds increases the potential as a result of the strong polarization of oxygen ions toward the X cation, which lowers the covalency of the M−O bond. Research shows that most lithium metal phosphate and sulfate compounds containing FeO_6 octahedra as the redox center have potentials in the range of 2.8−3.5 V versus Li/Li^+.[4] The advantage in using iron-based compounds is that, in addition to being naturally abundant and inexpensive, they are less toxic than vanadium, cobalt, manganese, and nickel compounds. The focus of the lithium battery community further intensified on this class of compounds with Pahdi et al.'s report on the electrochemical properties of $LiFePO_4$.[5] $LiFePO_4$ satisfies many of the criteria for an electrode material in a Li-ion battery: it can reversibly intercalate Li at a high voltage (3.5 V), and has a gravimetric capacity (170 mAh/g) which gives a cell made of the material a high energy density. The material is stable against overcharge or discharge, and is compatible with most electrolyte systems.[6,7] $LiFePO_4$ is also environmentally friendly, for it is found in nature as the mineral triphylite and is made from plentiful elements, reducing its cost of production.

The structure of $LiFePO_4$ is shown in Figure 1 and falls into the category of olivines, consisting of a distorted hexagonal close-packed (hcp) oxygen framework with 1/8 of the tetrahedral holes occupied by P, and 1/2 of the octahedral holes occupied by various metal atoms (in this case Li and Fe). $LiFePO_4$ crystallizes in space group #62 (*Pnma*). Layers of FeO_6 octahedra are corner-shared in the *bc* plane and linear chains of LiO_6 octahedra are edge-shared in a direction parallel to the *b*-axis. These chains are bridged by edge and corner shared phosphate tetrahedra, creating a stable three-dimensional structure. The promise of $LiFePO_4$ as an electrode material has prompted many reports and debates on its physical properties including the nature of ionic and electronic conductivity, aliovalent cation doping, solid solution behavior, particle size effects, and surface coatings.

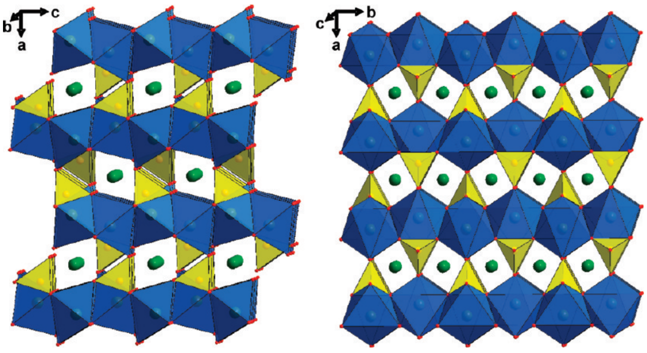

Figure 1. Polyhedral representation of the structure of $LiFePO_4$ (space group *Pnma*) viewed (a) along the *b*-axis and (b) along the *c*-axis. The iron octahedra are shown in blue, the phosphate tetrahedral in yellow, and the lithium ions in green.

Synthesis. Powders of lithium metal phosphates and silicates can be easily prepared by a variety of synthetic routes. The most common are solid-state methods in which precursors are ground or ball-milled together, with the resultant mixture being treated in a furnace. With iron compounds, inert gas or slightly reducing conditions are used to achieve an iron valence of Fe^{2+}.[5,8−24] Carbon-coated particles result from the use of carbon-containing precursors or the addition of organic compounds that decompose to carbon during thermalization. Sol−gel and solution deposition routes involve the mixing of appropriate precursors in solution, followed by drying and subsequent furnace treatment under an inert or reducing atmosphere.[25−31] When organic chelating agents are used to prepare the gel, a carbon coating is produced.

Low-temperature precipitation methods to prepare phosphates involve solution reflux. Crystalline $LiMPO_4$ can be precipitated from water,[32] polyols,[33,34] and ionic liquids.[35] Typically, nanoparticles result as the solvent acts as a stabilizer and growth inhibitor for the particles. Hydrothermal and solvothermal methods for synthesizing phosphates involve the partial dissolution of reagents in water or organic solvents in a sealed reactor heated to above 120 °C.[36−41] $LiMPO_4$ crystallizes under autogenous pressure, although at low temperature, site mixing of cations has been reported.[42,43] These reactions can be easily tailored to produce nanoparticles by the modulation of reaction temperature, concentration of precursors, and the addition of organic compounds to act as particle growth inhibitors. These low-temperature synthesis routes may be preferred as they are not energy intensive.

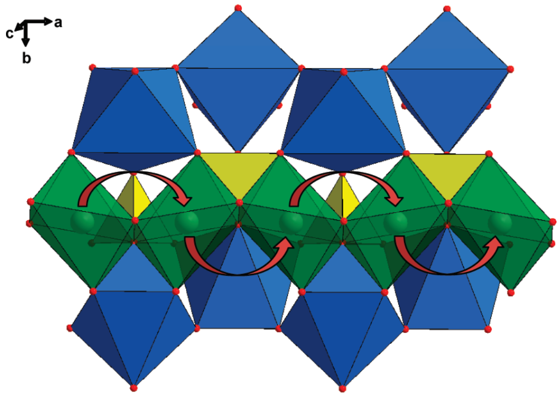

Figure 2. Structure of $LiFePO_4$ depicting the curved trajectory of Li ion transport along the *b*-axis, shown with red arrows. The color scheme is the same as in Figure 1.

Ion and Electron Transport. In the initial report of $LiFePO_4$, it was postulated that lithium diffusion could occur in two dimensions, as observed in $LiCoO_2$ and similar layered oxides.[5] The LiO_6 octahedra are edge-shared parallel to the *b*-axis of the crystal, creating Li tunnels in this direction. These chains are separated by octahedral interstitial sites along the *c*-axis, accounting for the second possible direction of Li transport. In 2004, Morgan et al. performed calculations to determine the diffusion coefficient of Li in Li_xFePO_4 ($x \approx 0$ and 1).[44] The results clearly indicate a preference for lithium ion transport along the *b*-axis. The diffusion coefficient was calculated to be several orders of magnitude higher in the [010] direction than the [001] direction. The activation energy for [010] lithium transport is also found to be 0.27 eV compared to 2.5 eV in the [001] direction for $LiFePO_4$. The high activation energy for this pathway is likely due to the octahedrally coordinated interstitial site which is face-shared with two PO_4 tetrahedra, causing cation occupation of this site to be highly unfavorable. As a result, the only significant Li transport was determined to be in the [010] direction.

Further structural modeling by Islam et al. confirmed the lowest energy pathway for Li transport is in the [010] direction, although a higher activation energy is calculated (0.55 eV).[45] Further simulations showed the migration between adjacent Li sites in the [010] direction did not occur by linear hopping, but rather along a curved pathway, as depicted in Figure 2. This result was confirmed by Nishimura et al. by performing maximum entropy method (MEM) modeling on neutron diffraction data of $Li_{0.6}FePO_4$ collected at 620 K.[46] The probability density of lithium nuclei was only observed in continuous curved pathways, via tetrahedral interstitial sites, along the [010] direction.

To test this result, measurements of ionic conductivity were carried out on single crystals of $LiFePO_4$. Li et al. performed AC impedance measurements on crystals grown by a flux method. Their results agree with the calculations of Morgan: the ionic resistivity along the [010] direction is about 1000 times less than that in the [100] direction and 3000 times less than in the [001] direction,[47] as seen in Figure 3a. Activation energies calculated from variable temperature impedance data were 0.636 eV [100], 0.54 eV [010], and 0.669 eV [001]. Although the activation energy is lowest in the [010] direction, the activation energies along the other two axes are found to be much smaller than calculated values.

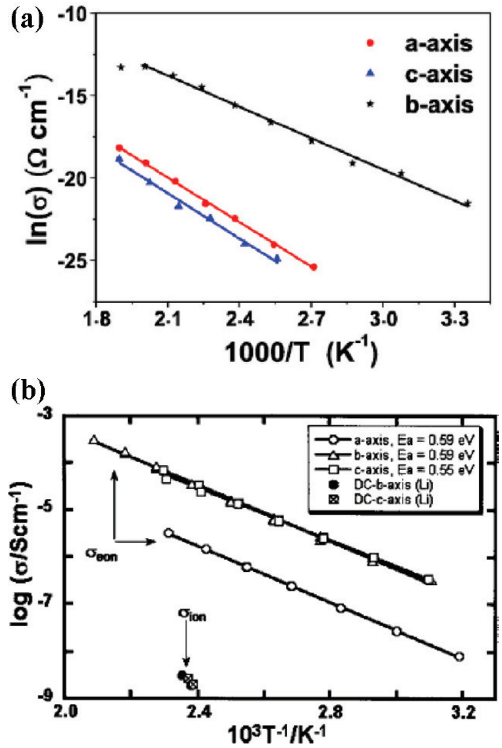

Figure 3. (a) Temperature-dependent ionic conductivity data from a single-crystal of $LiFePO_4$. Reprinted from reference 47, Copyright 2008, with permission from Elsevier. (b) Temperature-dependent total (electronic + ionic) conductivity and ionic conductivity from single-crystal $LiFePO_4$. Reprinted from reference 48, Copyright 2008, with permission from Elsevier.

Another study by Amin et al. reports on the conductivity of single-crystal $LiFePO_4$ grown by an optical floating zone method. Using titanium as ion-blocking electrodes, the total conductivity of each axial orientation of the crystal was measured. The results are shown in Figure 3b. Across the temperature range, the conductivity in the [010] and the [001] direction is more than 1 order of magnitude higher than that for the [100] direction.[48] This indicates electron conduction preferentially occurs in the *bc*-plane. The activation energy for electron hopping is reported to be about 0.6 eV for each orientation. Ionic conductivity, measured with electron-blocking electrodes, is much lower in magnitude (roughly 1×10^{-9} S/cm at 147 °C). The chemical diffusion coefficient of Li is determined to be 1.6×10^{-9} cm^2/s at this temperature. The fact that the magnitudes for ionic conductivity in both the [010] and [001] directions and the diffusion coefficient were found to be the same at 140−147 °C indicates two-dimensional Li transport must occur at that temperature, contrary to the aforementioned reports on one-dimensional transport. Furthermore, the total conductivity measurements denote the two-dimensional nature of the electronic conductivity in this crystal.

$LiFePO_4$, like many transition metal oxides, is considered to be a small polaron material in its mixed valent state accessed by partial oxidation. The charge carriers could be either holes in the case of $Li_{1-y}FePO_4$, or electrons in the case of Li_xFePO_4. The migration barrier of free polarons in purely stoichiometric $LiFePO_4$ and $FePO_4$ were calculated to be 0.215 and 0.175 eV respectively, using GGA methods.[49] However, long-range electrostatic interactions were calculated for a single Li^+ ion and an electron in $FePO_4$. The activation energy for this isolated transport is, in contrast, 0.37 eV. Alternatively, a similar study for a hole polaron and a lithium vacancy in $LiFePO_4$ revealed a binding energy over 0.5 eV. These values are much larger than those for free polaron transport and suggest that transport in these materials is highly coupled. Further evidence of highly coupled lithium ion/electron transport is observed upon the formation of high-temperature solid solution regimes of partially delithiated $LiFePO_4$. The onset of lithium disorder in these materials is found to be 220 °C,[31] the same temperature at which rapid electron hopping commences.[50a]

Unlike the conductive metal oxides, the electronic conductivity of $LiFePO_4$ is about 1×10^{-9} S/cm at room temperature,[51] limiting electrochemical performance because electrons cannot easily transport through the material. The nature of the ionic conductivity has been debated, although it is widely accepted that lithium-ion transport and hopping of small polarons are highly coupled.

Mechanisms of Delithiation. In the initial report of the electrochemical properties of $LiFePO_4$, it was noted that the electrochemical profile remained flat over a large compositional range.[5] These data indicated that both the extraction and insertion reactions proceeded by the motion of a two-phase interface. The second phase was identified to be orthorhombic $FePO_4$, which crystallizes in the same space group as $LiFePO_4$ (*Pnma*). The difference in unit-cell volume between the two phases was found to be 6.8%. Furthermore, the initial report proposed a simple shrinking core model to describe the intercalation of Li into $FePO_4$ where lithium insertion proceeds from the surface of a particle moving the two-phase interface. As a consequence, a critical phase-boundary surface area may be reached where the rate of lithium transported across the interface is not able to sustain the applied current. Thus, ion transport becomes diffusion-limited. Using this basis, electrochemical profiles of cells discharged at various rates were successfully modeled.[52]

However, the nature of lithium-ion transport in $LiFePO_4$ is highly anisotropic, and most reports above predict it is confined to tunnels along [010]. First-principles calculations of surface energies and surface redox potentials showed the (010) and (201) surfaces to be the lowest in energy and thus the Wulff shape of $LiFePO_4$ resembles a diamond-shaped platelet, similar to crystallites typically produced by hydrothermal reactions.[53] Furthermore, calculations show the (010) surface has a lower potential compared to bulk $LiFePO_4$ (2.95 V vs 3.55 V), suggesting that Li will be extracted from the (010) surface first upon charging the electrode material. As the (010) surface is initially deintercalated and this facet is the terminus of the 1D Li channels in the material, the maximization of its surface area would be key to the optimization of $LiFePO_4$ electrodes. A further study modeled three common morphologies found by electron microscopy images and also found each particle shape to be dominated by the (010), (201), (011), and (100) surfaces.[54] The equilibrium shape in this study was determined to be isometric and somewhat rounded.

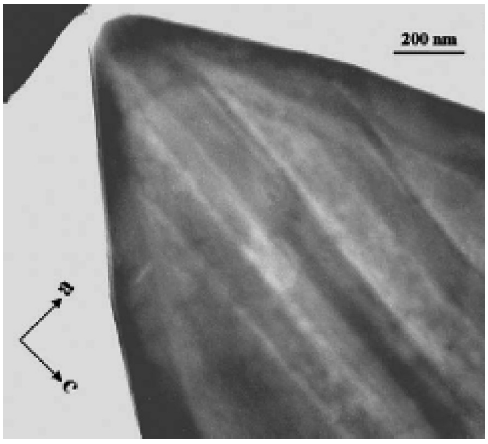

Figure 4. TEM micrograph of a hydrothermally prepared $Li_{0.5}FePO_4$ crystal, showing the domains of $LiFePO_4$ and $FePO_4$ aligned along the *c*-axis. Reproduced with permission from reference 55. Copyright 2006 The Electrochemical Society.

Moreover, partially oxidized $LiFePO_4$ large particles prepared hydrothermally by Chen et al. were shown to have ordered domains of $FePO_4$ situated between domains of $LiFePO_4$.[55] A TEM image of the (010) surface (i.e., the *ac* plane) is shown in Figure 4. Individual domains of $LiFePO_4$ and $FePO_4$ stretch approximately 100 nm in the [100] direction while separated by dislocation lines that ran in the [001] direction. The narrow dislocations between the crystalline phases were anticipated to exhibit a compositional gradient that allowed the two phases, $LiFePO_4$ and $FePO_4$, to coexist and maintain short-range order.

An electron energy loss spectroscopy (EELS) study of 130−170 nm particles prepared by a precipitation route was conducted by Laffont et al. EELS data on the O−K edge of a particle from a bulk sample delithiated to $Li_{0.45}FePO_4$ proved the core of the particle comprised $FePO_4$, whereas areas of the particle closer to the surface are $LiFePO_4$,[56] as shown in Figure 5. The spectra taken at the interfaces between these regions could all be represented with linear combinations of the spectra from $LiFePO_4$ and $FePO_4$. From these data, it was concluded that the interface is in fact a concurrence of the two phases and not a solid solution. For a particle with a composition of $Li_{0.75}FePO_4$, a small region of $FePO_4$ was detected under the surface $LiFePO_4$, although the $FePO_4$ was not located at the center of the particle core. On the basis of these observations, a mechanism for delithiation was proposed wherein upon nucleation, Li^+ and electrons

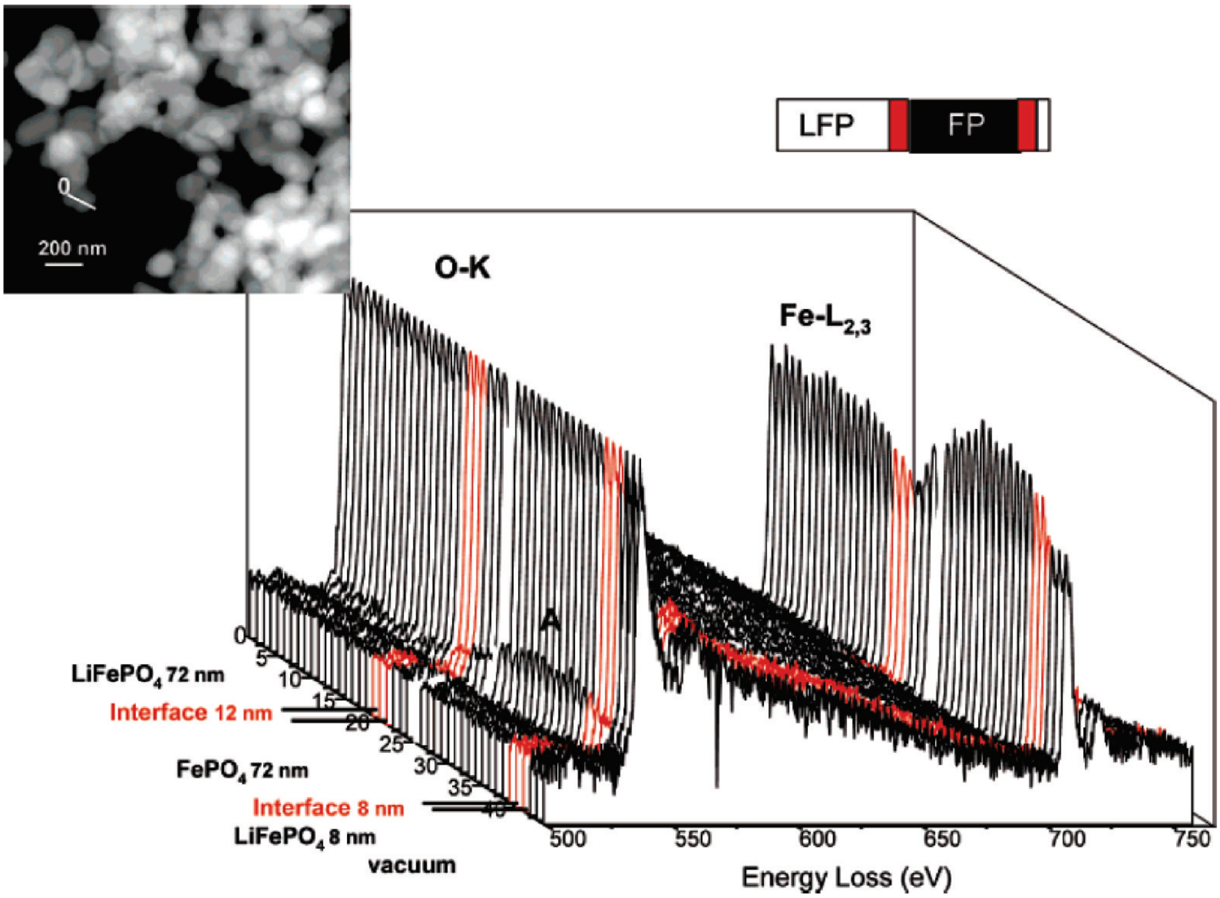

Figure 5. STEM image of the chemically delithiated sample $Li_{0.45}FePO_4$ with the line analysis and the 3D representation of EELS spectra recorded along that line. Domains of $LiFePO_4$ were found at the particle surface. Reproduced with permission from reference 56. Copyright 2006 American Chemical Society.

are removed from the *b*-axis tunnels based on two factors: (1) the number of Li^+/electron pairs displaced by hopping: shortest and most empty tunnels should delithiate first, and (2) the energy gain due to the proximity of the growing $FePO_4$ nucleus, thus minimizing the area and number of grain boundary interfaces. As delithiation progresses, the $FePO_4$ core formed in the particle interior extends in the *a*-direction through the entire particle. The process is effectively reversed for the case of relithiation. On the basis of this model, reduction of particle dimension in not only the [010] direction, but in all crystal directions is critical for good electrochemical performance.

A study on the partial electrochemical delithiation of smaller particles (< 100 nm in diameter) prepared by a classical solid state route was conducted by Delmas et al. High-resolution TEM images of selected partially electrochemically delithiated particles show the individual particles are single phase (either $Li_{1-y}FePO_4$ or Li_xFePO_4),[57] unlike the hydrothermal samples which exhibit clear regions of Li-rich and Li-poor phases.[55] The authors thus concluded when lithium deintercalation is nucleated, it proceeds very rapidly through the whole crystallite. To explain this phenomenon, a "domino-cascade" model was proposed: after a Li_xFePO_4 region is nucleated and a phase boundary is formed, the boundary moves rapidly in the *a*-direction (perpendicular to the direction of Li deinsertion). However, because of the difference in potential of particles on this scale, it is conceivable that redox reactions between larger deintercalated particles and pristine nanoparticles within the positive electrode itself could account for these TEM observations.[50b]

The various reported preparative methods of $LiFePO_4$ generate a vast array of particle morphologies. Consideration of the anisotropy of lithium ion transport within these morphologies and possible nanosize effects, combined with the inherent difficulty of imaging small iron phosphate particles, verifies the difficulty in determining a single global model that depicts the chemical and electrochemical reversibility.

Solid Solution Behavior. Although initial reports of $LiFePO_4$ described the electrochemical behavior as strictly two-phase in nature, solid-solution behavior has been observed at room temperature in the Fe^{2+}/Fe^{3+} region of $Li_x(Mn_yFe_{1-y})PO_4$, $y < x$.[58] The presence of manganese was thought to disrupt a weak transition metal association which stabilizes the $LiFePO_4/FePO_4$ phase boundary. Furthermore, an early model predicted the existence of two single compositional regimes, $Li_{1-y}FePO_4$ and Li_xFePO_4, close in composition to the end-members $LiFePO_4$ and $FePO_4$.[52] This was first confirmed experimentally by Yamada et al. X-ray diffraction studies on bulk particles of various compositions of the

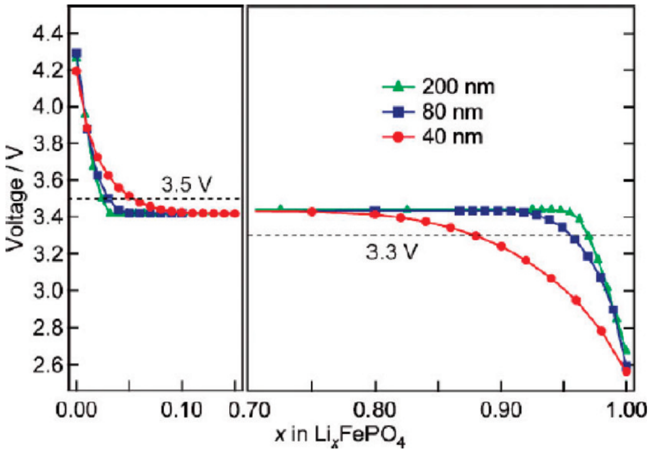

Figure 6. OCV curves measured for Li_xFePO_4 with various mean particles sizes of 200, 80, and 40 nm, showing the particle size dependence of the room-temperature miscibility gap. Reproduced from reference 63 with permission. Copyright 2009 Wiley−VCH Verlag GmbH & Co. KGaA.

chemically oxidized olivine confirmed the presence of two phases: a Li-rich phase with a unit cell volume of 290.7 Å^3, less than that of pure $LiFePO_4$ (291.1 Å^3) and a Li-deficient phase with a unit cell volume of 272.6 Å^3, greater than that of pure $FePO_4$ (271.9 Å^3).[59] Using Vegard's law, the limits of the solid solution were determined to be $Li_{1-y}FePO_4$, $y = 0.038$ and Li_xFePO_4, $x = 0.032$. A further study using neutron diffraction to determine lithium content shows the miscibility gap to be narrower, where $y = 0.11$ and $x = 0.05$.[60] These monophasic regions of the electrochemical curve are also found to stray from the constant value of 3.42 V seen for the two-phase transition. This miscibility gap is found to reduce upon decreasing particle size: values of $y = 0.12$ and $x = 0.06$ are obtained for 40 nm particles, as shown in Figure 6. Values of $y = 0.17$ and $x = 0.12$ are obtained for 34 nm particles.[61] Rietveld refinement of these nanoparticles shows a significant amount of stress within the lithium-rich and lithium-poor regions of the particles as a result of the averaged bond lengths for Fe^{2+}−O and Fe^{3+}−O within each phase. These coherence stresses are not seen for bulk particles. This effect has been explained previously by Wagemaker et al.[62] The coexistence of two crystallographic phases within one particle leads to a slight phase boundary energy penalty, mainly due to the difference in lattice parameters of the phases. Such a strain-induced energy can destabilize a two-phase coexistence in smaller particles, where the volume of the phase boundary is a significant fraction of the particle volume. As a result, the energetic benefits of phase separation will decrease for smaller particles and the miscibility gap will gradually narrow for particles of decreasing size.

Oxidation of $LiFePO_4$ upon exposure to air also results in the formation of Li_xFePO_4 solid solutions.[63] X-ray diffraction studies clearly indicate the reduction of the lattice parameters of the lithium-rich phase and Mössbauer spectroscopy indicates the formation of Fe^{3+} after one day of air exposure at room temperature. This effect is much more pronounced for particles < 100 nm in size. The particle size dependence of the miscibility gap was further confirmed by the isolation of pure $Li_{0.93}FePO_4$ obtained by chemical delithiation of 40 nm $LiFePO_4$.

The discovery of thermally activated solid-solution behavior over the entire compositional range of Li_xFePO_4 was made by Delacourt et al., based on temperature-dependent X-ray diffraction studies.[31] Results for a composition of $Li_{0.68}FePO_4$ are shown in Figure 7a. Peaks from the $Li_{1-y}FePO_4$ and Li_xFePO_4 phases present at room temperature begin to broaden near 210 °C and completely coalesce near 300 °C for most compositions, giving rise to a set of sharp reflections characteristic of new Li_xFePO_4 phases. Upon cooling, these newly formed high-temperature phases demix into $FePO_4$, $LiFePO_4$, and other metastable Li_xFePO_4 phases, later determined to include $Li_{0.64}FePO_4$.[64] Examination of the X-ray diffraction data at 350 °C reveals the presence of a single olivine phase for all compositions. The unit-cell parameters at this temperature for each stoichiometry roughly follow Vegard's law. Various compositions were analyzed, allowing for the construction of a temperature-dependent phase diagram. Neutron studies at high temperature showed that the solid-solution phases had Fe−O and Li−O bond distances intermediate between those of the end-members $LiFePO_4$ and $FePO_4$. Furthermore, no ordering of the lithium ions is detected. Temperature-dependent Mössbauer spectroscopy of partially delithiated $LiFePO_4$ shows the presence of two doublets, typical of Fe^{2+} and Fe^{3+} at room temperature. Near 200 °C, an intermediate iron valence state is formed. The Mössbauer data for $Li_{0.55}FePO_4$ is summarized in Figure 7b. The development of this intermediate valence is accompanied by the diminution of the parent Fe^{2+} and Fe^{3+} signals upon further heating.[50a] In this thermally excited state, the Fe−O bond lengths in the $Fe^{2+}O_6$ and $Fe^{3+}O_6$ sites become transiently equivalent, permitting the electron hopping to occur in a concerted manner over a large lattice domain. This resultant electron delocalization over the entire lattice on the Mössbauer time scale occurs for several compositions. As the onset of lithium disorder occurs at essentially the same temperature as electron delocalization, it is expected that these two phenomena are highly coupled. Furthermore, these high-temperature solid-solution phases can be quenched and studied at room temperature. X-ray diffraction shows the lithium remains disordered in the lattice but Mössbauer data shows that the iron valence states are static on the Mössbauer time scale.[65] The resultant phase diagram based on several quenched Li_xFePO_4 compositions is similar to that reported by Delacourt et al.[31] and a composition of $Li_{0.6}$FePO4 was found to be stable at relatively low temperatures.[66] Reheating the quenched samples back up to 140 °C caused a small fraction of electrons to disorder on the Mössbauer time scale, a much lower temperature than for the two-phase mixture indicative of faster intrinsic electron transport in the disordered sample, likely a result of lithium ion disorder.

Highly defective $LiFePO_4$ phases were prepared by Gibot et al. by a low-temperature precipitation method.

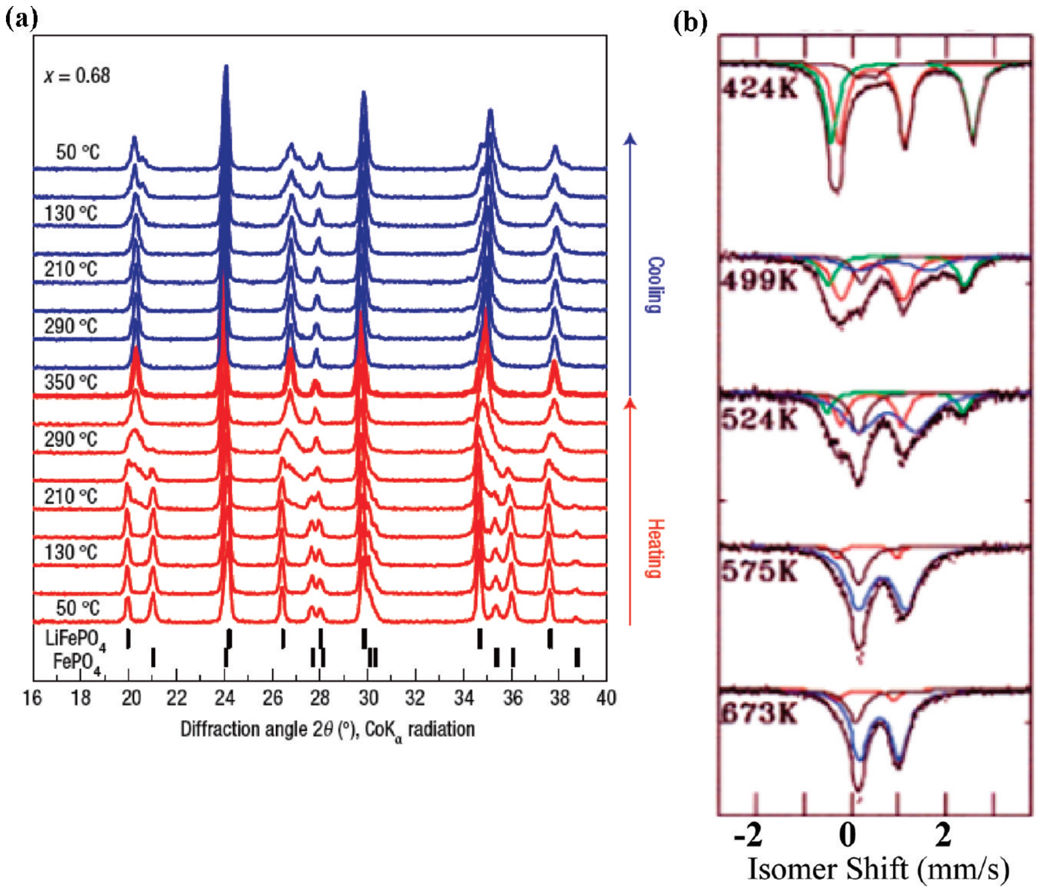

Figure 7. (a) Temperature-controlled XRD patterns (Co Kα) of $Li_{0.68}FePO_4$ under N_2.Reprinted by permission from Macmillan Publishers Ltd. from reference 31, copyright 2005. (b) Temperature-dependent Mössbauer spectra of $Li_{0.55}FePO_4$. The solid lines (green, Fe^{2+}; red, Fe^{3+}; blue, solid solution) are individual components that contribute to the overall fitting of the spectra. Transformation of each of the two-phase samples into Li_xFePO4 single phases is initiated at 200 °C, and completed at 350 °C.

Chemical analysis revealed substantial deviations from typical olivine stoichiometry for both 70 nm samples ($Li_{0.89}Fe_{0.96}PO_4$) and 40 nm samples ($Li_{0.79}Fe_{0.969}PO_4$).[67] Mössbauer measurements disclose the presence of Fe^{3+} in each of the samples, although insufficient amounts of Fe^{3+} were found to properly balance the stoichiometry (given the stoichiometry, 35% Fe^{3+} should be present in the 40 nm sample and only 22% was found). Rietveld analysis showed 15% vacancies on the M1 site, 10% vacancies on the M2 site, and showed Li/Fe antisite mixing (6% Fe on M1 sites) occurs during synthesis, common with synthetic methods where the temperature is below 120 °C.[42] Even with the Li channels partially blocked by iron ions and only having a stoichiometry of 0.79 Li, 82% of the theoretical capacity of $LiFePO_4$ was reportedly obtained. The electrochemical curve had a sloping profile, indicative of solid-solution behavior in the material. Although the result is interesting, more insight is needed into the precise stoichiometry, the role of defects, and nature of ionic conductivity in this $LiFePO_4$-like material.

The size-dependent nature of the miscibility gap has been well-established for $LiFePO_4$. It is uncertain what the critical particle size is for the full removal of this gap. Stoichiometric 30−40 nm particles of $LiFePO_4$ exhibit two-phase behavior over 70% of the composition range, while highly defective materials of the same particle size seem to exhibit solid-solution behavior over the entire composition range, although the precise stoichiometry of this phase is not certain. Clearly, the synthetic procedure plays a role in the formation of lattice defects that may increase ionic conductivity in these materials.

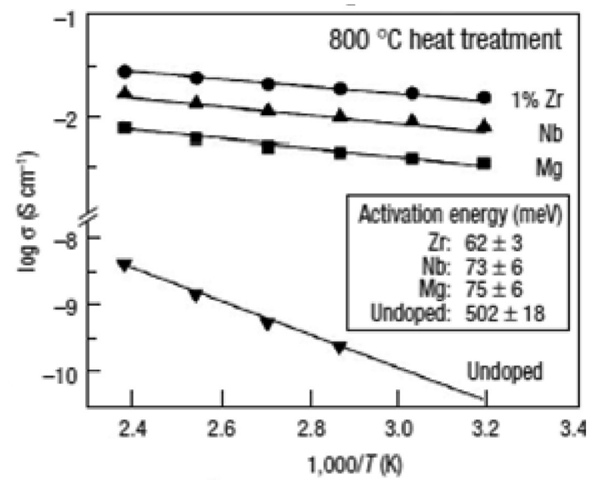

Figure 8. Temperature-dependent DC conductivity plots on pressed pellets of $LiFePO_4$ and various doped compositions of the type $Li_{1-x}M_x$-$FePO_4$, sintered at 800 °C. Reprinted by permission from Macmillan Publishers Ltd. from reference 51, copyright 2002.

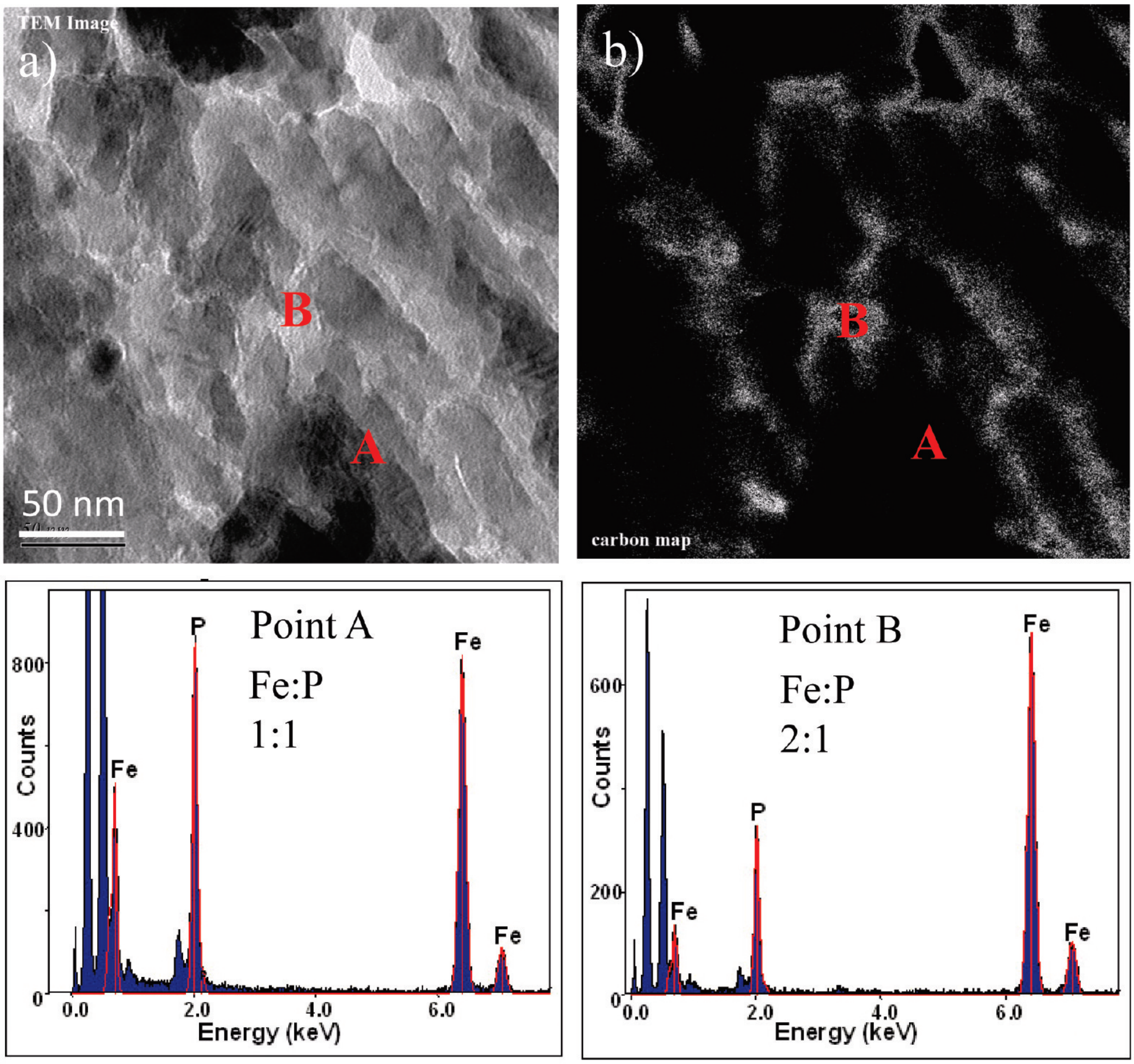

Figure 9. (a) TEM image and (b) carbon map from a sample of $Li_{0.90}Zr_{0.01}FePO_4$, along with TEM EELS data from two points on the sample. Point A ($LiFePO_4$ particle) exhibits a 1:1 Fe:P ratio, corresponding to $LiFePO_4$. Point B (grain boundary) exhibits a 2:1 Fe:P ratio, corresponding to the formation of metallic Fe_2P. Regions of Fe_2P are connected by the carbon, creating a conductive "nano-network".

Aliovalent Doping. Cation doping in oxide materials is a very commonly reported phenomenon and a very intriguing report on aliovalent cation doping of $LiFePO_4$ was published by Chung et al. in 2002. Compounds of the type $Li_{1-x}M^{z+}{}_xFePO_4$ ($z \geq 2$), sintered at 800 °C, were found to have exceptional electronic conductivity, more than 1×10^8 times higher than in pure $LiFePO_4$.[51] Data for selected doped compositions are shown in Figure 8. Although this stoichiometry strictly implies the iron valence would be less than Fe^{2+}, charge compensation by Fe^{3+} was postulated as the basis of the dramatic conductivity increase. Although the dopant was thought to reside on the lithium (M1) site and create additional lithium vacancies, no crystallographic evidence of the presence of dopants in the lattice was presented. This sparked debates over the source of the increased conductivity, the presence of dopants in the lattice, and the sustainability of lithium vacancies in the structure.

A subsequent study reveals poor conductivity of Zr- and Nb-doped $LiFePO_4$.[68] The conductivity increases only when additional carbon is added. Carbon-containing precursors, as carbon or which decomposed to produce metallic species, were thus deemed to be the source of high conductivity in the Chung material. Other studies of high-temperature lithium-deficient doped and undoped $LiFePO_4$ that followed found similarly highly conductive compounds[69,70] to Chung et al.[51] Electron energy loss spectroscopy revealed a high Fe:P ratio in the grain boundaries in addition to carbon (see Figure 9), indicative of metallic iron phosphides or iron phosphocarbides. The phosphides are produced by carbothermal reduction of $Fe_2P_2O_7$ or $LiFePO_4$. Carbon makes a percolating conductive network through the sample with the phosphides, which accounted for the increase in conductivity. X-ray diffraction analysis probing the presence of small dopant quantities in the $LiFePO_4$ lattice was inconclusive. In the presence of small quantities of carbon, pure $LiFePO_4$ could also be made conductive; carbon-free doped and undoped materials exhibited no increase in conductivity. A further study by Delacourt et al. on Nb-doped $LiFePO_4$ reveals only samples prepared with high carbon content are found to be highly conductive.[71] Furthermore, crystalline β-$NbOPO_4$ was detected on the surface of the olivine particles, further questioning the validity of doping claims.

Calculations by Islam et al. further question the possibility of doping olivines.[45,72] Defect simulations on $LiFePO_4$ demonstrated the accommodation of an aliovalent dopant on either the M1 or M2 site is highly unfavorable. Based on energetics, there is also no highly valent cation which prefers to occupy the M1 site, the dopant site proposed by Chung et al. However, X-ray diffraction studies on doped olivines with lithium substoichiometry charge compensated by dopant concentration, $Li_{1-3x}Fe^{3+}{}_xMgPO_4$ and $Li_{1-3x}Fe^{3+}{}_xNiPO_4$, revealed that substantial doping ($x < 0.15$) could be sustained in the magnesium and nickel olivines.[73,74]

The debate over the presence of dopants in the $LiFePO_4$ lattice was revisited by Wagemaker et al. in 2008. Combined refinement of X-ray and neutron diffraction data was carried out on compounds with various dopant stoichiometries.[75] Refinements of target compounds similar to those reported by Chung et al. (i.e., $Li_{1-x}M^{z+}{}_xFePO_4$) show a preference of the dopant to occupy the M1 site, although the quantity of dopant in the lattice is much less than targeted. In contrast, target compounds with charge-compensated stoichiometries (ie. $Li_{1-zx}M^{z+}{}_xFePO_4$, $x \leq 0.03$) are found to incorporate roughly all of the dopant, again with a preference for doping on the M1 site. At higher dopant concentrations, impurities are clearly detected by diffraction. Most importantly, the refinements show the incorporation of the aliovalent dopant is balanced by lithium vacancies, resulting in the charge of the iron ion in the lattice to remain at +2.00, ruling out the presence of Fe^{3+} holes. The resultant vacancies (9% for $Li_{0.88}Zr_{0.03}FePO_4$) are determined to be entirely localized on the M1 sites. Compositions that stabilize a high concentration of vacancies exhibit a larger unit-cell volume as a result of oxygen–oxygen repulsion at the vacant M1 sites. A further study by Chiang et al. claims up to 12% Zr doping in $LiFePO_4$, although the authors admit large quantities of Zr-containing phosphates were also detected by X-ray diffraction.[76] Thus it could be concluded that the lattice was not doped to this large extent.

The nature of the dopant lattice site, doping limits, the resultant physical properties, and even the very existence of aliovalent doping of $LiFePO_4$ has been rigorously debated in recent years. Crystallographic evidence has shown the presence of small quantities of dopants in $LiFePO_4$ (typically less than 3%) if the target stoichiometry is properly charge balanced although these doped compounds do not exhibit increased conductivity, as the iron valence remains Fe^{2+}. However, the presence of an immobile ion in the lithium channels would likely hinder lithium transport, assuming one-dimensional transport.

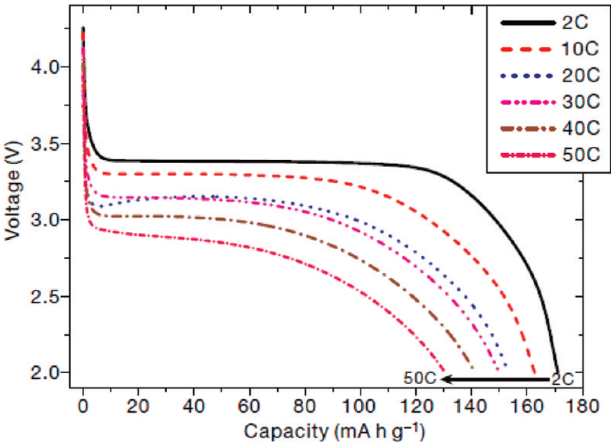

Figure 10. Discharge rate capability for $LiFe_{0.9}P_{0.95}O_{4-\delta}$ synthesized at 600 °C. Cells charged at *C*/5 and held at 4.3 V until the current reaches *C*/60. *C*/*n* denotes the rate at which a full charge or discharge takes *n* hours. The loading density of the electrode is 3.86 mg/cm^2. Reprinted by permission from Macmillan Publishers Ltd. from reference 78, copyright 2009.

Surface Modifications of $LiFePO_4$. With the general failure to modify the intrinsic properties of $LiFePO_4$ by doping, recent reports of improving the performance of $LiFePO_4$ as a positive electrode material in lithium ion batteries have come about as a result of the intensive study of surface coatings. When stoichiometries $Li_{1-x}FePO_4$ or $Li_{1-x}Zr_xFePO_4$ are targeted, $Fe_2P_2O_7$ is found to form as an impurity, which undergoes carbothermal reduction at 800 °C.[69] As a result, the surface of $LiFePO_4$ particles can be made conductive by the in situ generation of a nanonetwork of conductive iron phosphide and carbon. Studies have shown improvements to electrochemical performance by the production of metallic phosphide coatings on the surface of $LiFePO_4$.[77]

Conversely, to improve the ionic conductivity of the surface, stoichiometries of the type $LiFe_{1-2x}P_{1-x}O_{4-y}$ were prepared.[78] The substoichiometry of iron was designed to produce an ionically conductive lithium phosphate glasses on the particle surface. Analysis of the surface coating revealed it is a phase similar to $Li_4P_2O_7$, although it could contain some FeP or Fe^{3+}. The material exhibited exceptional capacity at high rates: 140 mA h/g was achieved for a cell discharged in 3 min (20*C* rate), as shown in Figure 10. When the electrode material is prepared with 65% mass of carbon, a capacity of more than 100 mA h/g is achieved at a very fast rate of 200*C* (discharge in 18 s). The practicality of this data is questioned by Zaghib et al., who claimed that such high quantities of carbon would lower the energy density of a practical cell.[79] The challenge with a practical lithium-ion cell is the reduction of the charge time: it would be impossible to charge a cell at such high rates because of performance limitations of negative electrode materials and safety concerns over the growth of lithium dendrites shorting the cell and the production of heat due to the internal resistance of a battery. The nature of the coating is also disputed. Zahgib et al. claimed the conductive coating could not be the insulating $Li_4P_2O_7$, but is likely carbon. The Fe^{3+} detected is likely due to surface oxidation seen previously.

Figure 11. TEM image of $LiMnPO_4$ nanoparticles synthesized by the polyol route. Reprinted from reference 86, Copyright 2009, with permission from Elsevier.

There are many previous reports on coating $LiFePO_4$ particles with carbon in order to improve the conductivity and electrochemical performance. A report in 2004 compared the types of carbon produced from various organic additives and found improved performance from $LiFePO_4$ containing high sp^2 carbon content, derived from organic compounds that contained a high percentage of sp^2-hybridized carbon.[27,80] Additionally, a thick carbon coating may be detrimental to electrode performance.[81] Carbon reduces the volumetric energy density to a point where cells with this material would be impractical for common applications. As such, it is important to maximize conductivity and minimize carbon content.

$LiMnPO_4$. The olivine $LiMnPO_4$ is isostructural with $LiFePO_4$ and has a similar theoretical electrochemical capacity (170 mAh/g). Despite the higher voltage of $LiMnPO_4$ (4.1 V vs. Li),[5] few promising reports on the electrochemistry of compound have been published. The voltage profile during both charge and discharge of $LiMnPO_4$ is flat, implying that the conversion between $LiMnPO_4$ and $MnPO_4$ proceeds by a two-phase process. Difficulties with the $LiMnPO_4$ system arise from very low electrical conductivity and structural distortions upon oxidation to $MnPO_4$ which hinder ionic transport. As a result, many initial electrochemical reports of the material show poor capacity as well as very poor reversibility.[82−84]

Many recent reports have focused on reduction of particle size to improve transport properties and carbon addition to improve surface conductivity. Drezen et al. clearly demonstrates the benefits of reduced particle size on electrochemical performance of sol−gel prepared $LiMnPO_4$.[85] Wang et al. used a polyol method to produce crystalline nanoparticulate $LiMnPO_4$ at 200 °C.[86] The resultant particles were exceptionally thin, <30 nm in the *b*-direction (see Figure 11): this desirable morphology allows for a high discharge capacity to be reached in a short period of time (113 mA h/g in 1 h). Furthermore, the stable cycling of this material over 200 cycles proves the Jahn−Teller effect from the Mn^{3+} ion does not degrade the material as in the case of the spinel $LiMn_2O_4$. Phosphide surface coatings produced via carbothermal reduction have been shown to enhance the surface conductivity and electrochemical performance of $LiFePO_4$; however, it has been shown that carbothermal reduction of $LiMnPO_4$ does not occur at temperatures below 1000 °C, thus making the production of surface phosphides difficult.[70] It was demonstrated that the use of elemental Mn as a precursor to making $LiMnPO_4$ produces Mn_2P at temperatures >900 °C. However, the particle size of such material made electrochemistry prohibitive.[87]

The volume difference between $LiMnPO_4$ and $LiMnPO_4$ is 9.5%, substantially more than that of the Fe olivine.[88] A study on divalent cation substitution in $LiMnPO_4$ showed that the volume difference between lithiated and delithiated phases could be reduced to 7.8% for $LiMn_{0.9}Mg_{0.1}PO_4$, because of the retention of lithium ions in the delithiated phase in the presence of redox inactive magnesium.[88] The magnesium also stabilizes the Jahn−Teller distortions of the delithiated phase. As a result, electrochemical performance of $LiMnPO_4$ could be improved without the addition of a conductive additive.

Solid-solution behavior was found in Li_xMnPO_4 near full oxidation ($x < 0.2$).[89] Although the $LiMnPO_4$ particles were "sub-micrometer", the domains of the solid solution regime were determined to be <45 nm, suggesting that many domains coexist within the same particle. Lithium nonstoichiometry was not found for $Li_{1-y}MnPO_4$. A delithiation study by Kim et al. reveals the loss of morphology upon chemical delithiation of $LiMnPO_4$ and the appearance of small pores on the surface of the particles.[90] Efforts to observe a temperature-driven solid-solution regime for Li_xMnPO_4 ($0 < x < 1$) results in the partial decomposition of $MnPO_4$ to $Mn_2P_2O_7$ at 200 °C; no solid-solution behavior was observed. The degradation of particle morphology clearly indicates poor ionic transport in $LiMnPO_4$, which results from a large lattice mismatch between the lithiated and delithiated phases and Jahn−Teller distortions. The delithiated phase MnPO4 is also subject to the well-known disproportionation of 2 Mn (III) to Mn (II) + Mn (IV) (see below for further discussion of this process in spinels), which could result in dissolution. Further study into minimization of the lattice mismatch in $LiMnPO_4$, particle size reduction, and conductive surface coatings are key to the optimization of this promising material.

Fluorophosphates. Fluorophosphates are another class of electrode materials under scrutiny as potential lithium battery electrodes. Depending on the framework connectivity, these compounds may be expected to exhibit a high cell potential as a result of both the inductive effect of PO_4^{3-} group and the electron-withdrawing character of the F^- ion.

One of the first successful fluorophosphate materials was $LiVPO_4F$, reported by Barker et al.[91] This compound

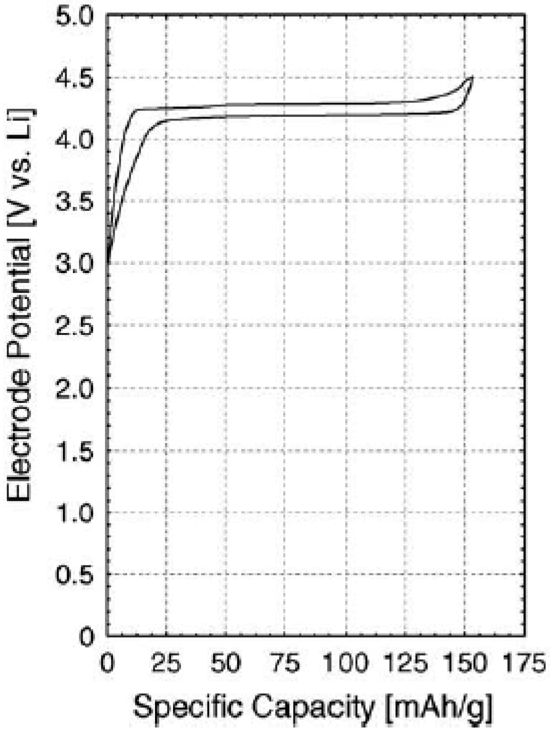

Figure 12. Electrochemical data for LiVPO$_4$F cycled between 3.0 and 4.5 V, showing the V^{+3}/V^{+4} redox couple at 4.2 V and the two-phase nature of delithiation. Reprinted from reference 94, Copyright 2005, with permission from Elsevier.

is isostructural with the minerals tavorite (LiFePO$_4$OH)[92] and amblygonite (LiAlPO$_4$F).[93] Lithium extraction and insertion is based on the reversibility of the V^{+3}/V^{+4} redox couple with the material exhibiting a two-phase plateau upon electrochemical cycling. The discharge potential of LiVPO$_4$F is determined to be 4.2 V vs Li. A subsequent study depicts the near-complete utilization of the theoretical capacity (156 mA h/g) at a slow rate of cycling, shown in Figure 12.[94]

Another lithium fluorophosphate material, based on the oxidation of V^{+3}, Li$_5$V(PO$_4$)$_2$F$_2$, is found to have a layered structure and could in theory span the entire range of V^{+3}/V^{+4}/V^{+5} redox couples.[95] The theoretical capacity of 170 mA h/g is similar to that of LiFePO$_4$. Initial results show complete lithium reversibility on the lower V^{+3}/V^{+4} redox couple, but the V^{+4}/V^{+5} transition is not found to be electrochemically reversible.

In 2005, the sodium vanadium fluorophosphate Na$_3$V$_2$(PO$_4$)$_2$F$_3$ was utilized as a positive electrode material in cells with metallic lithium or graphite as the negative electrode, along with a lithium salt electrolyte.[96] Sodium is deintercalated from the positive electrode upon the initial charge, resulting in a mixed alkali electrolyte composition. Sodium is believed to intercalate on discharge. The presence of sodium did not appear to degrade the electrolyte or the negative electrode, demonstrating the feasibility of lithium ion cells with sodium-containing electrode compounds. This key development vastly expanded the range of compounds which could be used in a lithium ion cell, especially with concerns over the global supply of economically recoverable lithium.

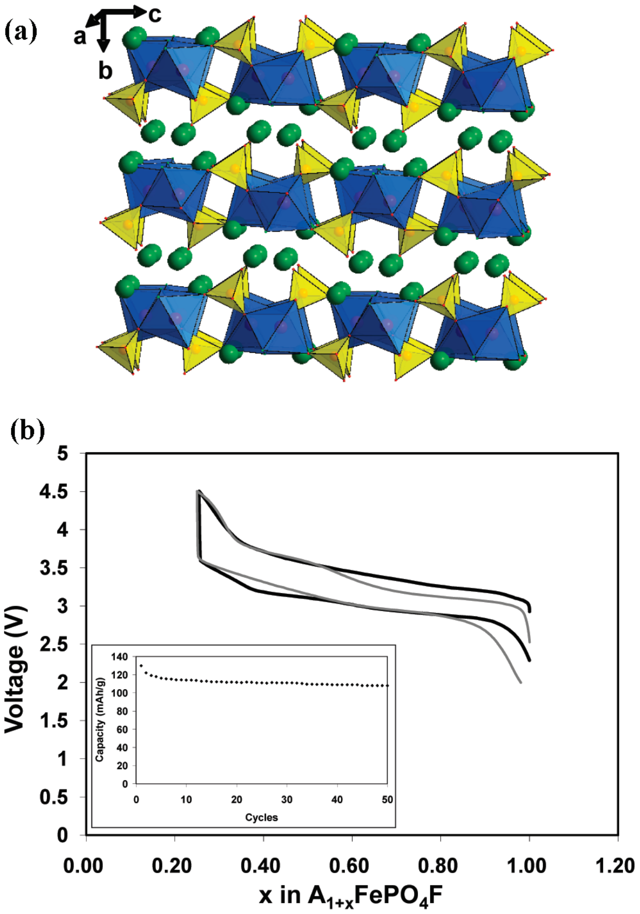

Figure 13. (a) Structural representation of Na$_2$FePO$_4$F. The iron octahedra are shown in blue, the phosphate tetrahedra in yellow, and the sodium ions in green. (b) First electrochemical cycle vs. Li of Na$_2$FePO$_4$F (shown in black) and Li$_2$FePO$_4$F (shown in gray). Inset: The electrochemical cycling stability of a cell comprised Na$_2$FePO$_4$F cycled vs metallic Li which shows little capacity fading.

In 2007, a new sodium iron fluorophosphate (Na$_2$FePO$_4$F) was introduced,[97a] with a structure similar to that of previously reported Na$_2$CoPO$_4$F[98] and Na$_2$MgPO$_4$F.[99] The compounds crystallize in the orthorhombic *Pbcn* space group (#60). The layered structure, shown in Figure 13a, has several interesting features: corner-sharing of face-shared dimers of octahedral Fe^{2+} sites and [6 + 1] co-ordination of both crystallographically unique sodium sites.

Initial deintercalation of Na$_2$FePO$_4$F proceeds through a quasi-solid solution regime wherein Na$_{2-x}$FePO$_4$F ($x < 0.5$) compositions are found to be single phase and the *Pbcn* structure is maintained. The composition Na$_{1.5}$FePO$_4$F is found to undergo a slight distortion to a monoclinic unit cell. Further oxidation restores the orthorhombic structure. The unit-cell volume of the NaFePO$_4$F end-member (818.48 Å^3) is only 4% less than that of Na$_2$FePO$_4$F (854.93 Å^3). The transition between these two closely related phases is a lower strain process than that in LiFePO$_4$, where the unit-cell volume difference between the lithiated and delithiated end-members is roughly 6.7%. As a result, Na$_2$FePO$_4$F exhibits solid-solution-like electrochemical character. The sodium on the Na2 site is totally removed upon full oxidation, with

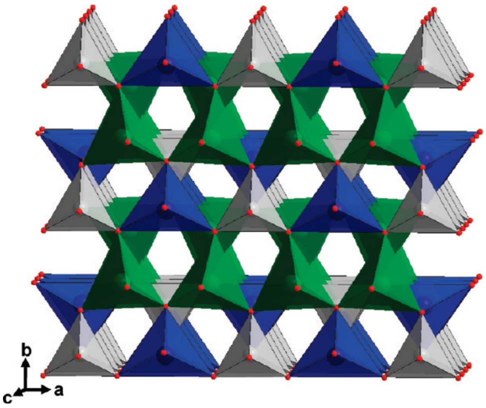

Figure 14. Structural representation of Li_2FeSiO_4. The iron tetrahedra are shown in blue, the lithium tetrahedra in green, and the silicate tetrahedra in gray.

Na1 still fully occupying the layers. Thus the Na2 network of sites is considered the ion mobility pathway in the structure. Although this material could be used in a sodium cell with an appropriate negative electrode, initial electrochemical tests of this material were run in a hybrid-ion cell *vs.* Li. About 80% of the theoretical capacity (135 mAh/g) is attained on the first cycle and little capacity fading is observed over 50 cycles. The average potential is 3.5 V, comparable to that for $LiFePO_4$. On discharge, lithium is found to intercalate into the material. Successive cycling of the material shows the sodium content decreases to roughly 20% of the original compound, indicating some exchange between the Na2 and Na1 site occurs. This is not surprising, as each Na2 site face-shares with three Na1 sites. Li_2FePO_4F is obtained via ion exchange of Na_2FePO_4F with LiBr. The voltage profiles of both Na_2FePO_4F and Li_2FePO_4F vs. Li are shown in Figure 13b. Both Na_2FePO_4F and Li_2FePO_4F display sloping voltage profiles, indicative of solid-solution behavior. Na_2FePO_4F exhibits excellent reversibility up to 50 cycles.[97b]

Although other fluorophosphates with this A_2MPO_4F (A = alkali metal, M = transition metal) stoichiometry are known, it is remarkable that three different structure types exist because of effects of cation size and magnetic spins. The layered structure of Na_2FePO_4F and Na_2CoPO_4F differ greatly from the structure of Na_2MnPO_4F,[100] which comprises corner-shared manganese octahedra and phosphate tetrahedra with sodium residing in tunnels and that of Li_2NiPO_4F[101] and Li_2CoPO_4F[102] in which the metal octahedral are edge-shared and lithium ions reside in layers. Li_2CoPO_4F was found to be electrochemically reversible, although Li_2NiPO_4F likely has redox potential above the range of stability for most electrolytes. Despite the synthesis of carbon-coated nanoparticles, Na_2MnPO_4F was found to be electrochemically inactive.[97b]

Fluorophosphate materials, notably $LiVPO_4F$ and the solid-solution-like Na_2FePO_4F, show great promise as electrochemical storage materials. Furthermore, the ability to use sodium compounds directly in a lithium ion cell is advantageous in terms of processing cost and lithium availability and allows the study of new compositions and architectures.

Silicates. With the success of phosphate materials, other polyanionic materials, namely silicates, have also been studied as positive electrode materials. Most of the silicates investigated are of the form Li_2MSiO_4 where M^{+2} is a transition metal. These silicates crystallize in various polymorphs, all of which are structurally similar to β-Li_3PO_4[103] or γ-Li_3PO_4[104] where all the cations occupy tetrahedral sites. The structure of Li_2FeSiO_4, first reported in 2005, is related to the former.[105] The quasi-layered structure is shown in Figure 14. Lithium ions occupy tetrahedral sites in between layers comprising chains of alternating corner-shared FeO_4 and SiO_4 tetrahedra, which run in the *a*-direction. In this report, all the FeO_4 and SiO_4 tetrahedra face the same upward direction. This was found not to be the case in a later study, where refinement of the structure showed alternating pairs of FeO_4 and SiO_4 tetrahedra face downward.

Li_2FeSiO_4 was shown to undergo an initial charge at 3.10 V vs. Li while subsequent charges were at 2.84 V vs. Li.[105] A reversible capacity of 140 mA h/g was displayed over 8 cycles. The decrease in voltage was attributed to a structural rearrangement after the first cycle where Li and Fe site exchange occurred.[106] The high voltage of the initial charge was later determined to be a result of an impurity, as pure Li_2FeSiO_4 is shown to deintercalate at a voltage of 2.8 V.[107] The measured electronic conductivity of Li_2FeSiO_4 is 3 orders of magnitude lower than for $LiFePO_4$.[108]

Li_2MnSiO_4, isostructural with Li_2FeSiO_4, is found to have a redox potential near 4.0 V.[109] Initial results show substantial irreversible capacity loss, even upon the synthesis of carbon-coated Li_2MnSiO_4 nanoparticles.[108-110] This is found to be the result of amorphization of the delithiated manganese silicate.[108] Calculations confirm the thermodynamic stability of four Li_2MnSiO_4 polymorphs that can be synthesized at various temperatures and pressures.[111] Four polymorphs of Li_2CoSiO_4 have been synthesized previously.[112] The electrochemical reversibility of three polymorphs of Li_2CoSiO_4 after the initial charge is found to be poor,[113] as is also the case for the corresponding Co^{2+} olivine phosphate, $LiCoPO_4$.[114,115]

The redox potentials of the aforementioned silicates are close to calculated values.[116] Not surprisingly, the calculated potentials of transition metal silicates with the Li_2FeSiO_4 framework are lower than those for the corresponding transition metal olivine phosphate owing to the inductive effect.

Li_2FeSiO_4 may be a promising electrode material but compared to $LiFePO_4$, the silicate exhibits lower electronic conductivity and a lower electrode potential albeit with a similar theoretical capacity. These shortcomings may limit the commercial usefulness of this compound.

3. Lithium Metal Oxide Positive Electrodes

No review of lithium-ion positive electrode materials would be complete without brief mention of $LiCoO_2$, the oxide that ostensibly started the field. First reported by

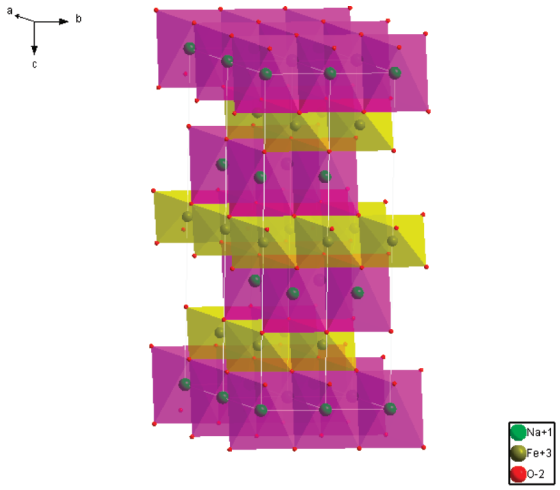

Figure 15. Structure of α-$NaFeO_2$ ($R\bar{3}m$).

Goodenough et al.,[117] it has received tremendous attention following its successful commercialization in 1991 and can be considered a "mature" material at this point although it has sustained several developments within the past decade that have produced very significant improvements. $LiCoO_2$ adopts the α-$NaFeO_2$ structure (Figure 15) with consecutive alternating CoO_2 and Li layers—thus Co^{3+} resides in the 3a site, and Li^+ in the 3b site in the $R\bar{3}m$ ccp packed O^{2-} lattice. Both Co and Li are octahedrally coordinated. The reaction mechanism of Li_xCoO_2 on Li extraction can be summarized as follows: first, an expansion of the interlayer c axis as a result of electrostatic repulsion of the oxygen layers $x \lesssim 0.5$;[118,119] second, a hexagonal-monoclinic transformation at $x \approx 0.5$ that represents an order—disorder transition.[118,120] Lastly, a transformation of the O3 $LiCoO_2$ phase (close-packed oxygen layers with an ABCABC stacking sequence) into the O1 Li_xCoO_2 phase (ABAB stacking sequence) occurs at $x \approx 0.05$.[119,121] The transformation proceeds via an intermediate phase, $Li_{0.12}CoO_2$, (H1−3)[122,123] a hybrid host structure that encompasses both the O3 and O1 stacking sequences. Although almost all of the Li can be extracted to give a theoretical capacity of 274 mA h/g, only a little over half of the capacity is practically reversible for insertion/deinsertion (≤4.2 V vs Li/Li^+). Capacity fading is severe upon extraction of >0.7Li because of loss of oxygen (resulting from reduced stability of lithium poor phases),[124] electrolyte decomposition,[125,126] and the problem of cobalt dissolution in typical electrolytes.[127] Doped variants $LiM_xCo_{1-x}O_2$ (M = Al,[128,129] Cr[130]) have proven quite successful in improving the electrochemical performance. Also, recently, Cho et al. reported improved reversible capacity with very good cycle performance by coating metal oxides[131] or phosphates[132] on $LiCoO_2$. They proposed that the volume strain of Li_xCoO_2 decreases as a result of the metal oxide coating, including zero strain with a ZrO_2 coating. Cho et al. also showed that $AlPO_4$-coating on $LiCoO_2$ improved the safety associated with overcharge.[132] Other factors have also been suggested. These include the amelioration of reactivity with HF that is formed by side reactions of the $LiPF_6$ electrolyte.[133,134] Nonetheless, alternatives to $LiCoO_2$ are necessary because of its high cost, toxicity, and poor safety that make it unsuitable for large-scale energy-storage applications.

Spinels. One such alternative is the spinel $LiMn_2O_4$, an appealing candidate as the more chemically stable $Mn^{3+/4+}$ couple offers excellent safety and high power capability owing to the 3D lattice. Furthermore, Mn is inexpensive and environmentally benign. $LiMn_2O_4$ exhibits an operating voltage of 4.1 V, and the couple for its high potential analogue, $Li[Ni_{0.5}Mn_{1.5}]O_4$, lies at about 4.7 V. The Li^+ ion occupies the tetrahedral 8d site in the cubic-closed packed O^{2-} lattice, and Mn^{3+} (or Ni^{4+}/Mn^{2+}), resides in the 16c octahedral site. Spinels have been the subject of exhaustive studies in the 1990s[135−137] that continue to the present day, which have highlighted the unusually facile Li^+ ion mobility in the framework, and the ability of the lattice to undergo substitution to enhance electrochemical properties. Like $LiCoO_2$, $LiMn_2O_4$ and its doped variants are now well-established commercial lithium-ion battery cathode materials. Their anticipated implementation as first-generation cathode materials for automotive applications is the result of greatly improved electrochemistry arising from a decade of crystal engineering, surface chemistry, and crystallite morphology optimization. A brief summary is provided here, which is by no means complete.

Spinel $LiMn_2O_4$ cathodes have been plagued by capacity fade, especially at elevated temperatures (> 50 °C). Several mechanisms such as Jahn—Teller distortion of Mn^{3+};[138] Mn dissolution into the electrolyte;[139] loss of crystallinity;[140] development of microstrain due to lattice mismatch between two distinct cubic phases formed on cycling;[141]and an increase in oxygen deficiencies or oxygen loss upon cycling[142] have all been suggested to be the source of capacity fade. Among them, dissolution of $LiMn_2O_4$ is almost universally considered to be the predominant cause. Acidic electrolytes, formed from hydrolysis of Li salts in organic electrolytes (i.e., HF released from $LiPF_6$),[143] will etch a $LiMn_2O_4$ electrode via a disproportionation reaction $2Mn^{3+} \rightarrow Mn^{2+} + Mn^{4+}$.[144] This has been confirmed by a recent study using first principles calculations to calculate the reaction free energy for dissolution.[145] It shows that doping of Li on the octahedral sublattice (to give $Li_{1+x}Mn_{2-x}O_4$) suppresses the exothermicity of the reaction by an amount akin to the dilution of trivalent Mn. Thus the dissolution of $LiMn_2O_4$, and strategies to mitigate it, have been the subject of extensive experimental research. Mn dissolution and other deleterious effects have been greatly inhibited by substitution of dopants into the spinel structure (i.e., $Li[Li_{0.1}Al_{0.1}Mn_{1.8}]O_4$)[146] by fluorine substitution for oxygen, oxide surface coatings, and electrolyte additives. Recent reviews outline some of these approaches.[147] An example of using both fluorine substitution, and layered metal oxides to act as proton traps and stabilize dissolution has been reported.[148] With some of the more practical aspects of Mn spinels at least partially resolved, recent attention has now turned to the generation of nanostructured materials to enhance electrochemical properties. For example, ordered mesoporous,[149] and nanorod morphologies[150] of $LiMn_2O_4$ have been recently described, with both exhibiting particularly high rate capability. Many studies have also been aimed at high voltage positive electrodes featuring the $Li[Ni_{0.5}Mn_{1.5}]O_4$ spinel,[151−154] which has also been prepared in a nanostructured morphology.[155] Coupled with an elevated-potential negative electrode such as the spinel $Li_4Ti_5O_{12}$, positive electrode spinel systems provide a route to an promising new generation of 12 V batteries, as described by Ohzuku et al.[156]

$LiNiO_2$. Isostructural $LiNiO_2$[157] was considered as an alternative to $LiCoO_2$ because of its lower cost, higher reversible capacity (ca. 200 mA h g^{-1}) and better environmental compatibility. However, it is difficult to synthesize stoichiometric $LiNiO_2$. The $Li_{1-y}Ni_{1+y}O_2$ phase is usually formed because the instability of the Ni^{3+} oxide favors conversion to 2y Ni^{2+} and $(1-y)$ Ni^{3+} with concomitant loss of yLi[158]. In turn, this gives rise to cation site disorder, since the occupation of Ni^{2+} is more favorable in the "interlayer" Li 3b site than Ni^{3+} because of the similar size of Ni^{2+} and Li^+ ($r_{Ni3+} = 0.56$ Å, $r_{Ni2+} = 0.69$ Å, $r_{Li+} = 0.76$ Å). Exchange of Li^+ and Ni^{2+} in the 3b and 3a sites results in materials that can be formulated as $[Li_{1-y-\alpha}\ Ni^{2+}_{y+\alpha}]$-$[Ni^{3+}_{1-y}Ni^{2+}_{y-\alpha}Li_{\alpha}]O_2$ (α: cation disorder between Ni^{2+} and Li^+, $\alpha < y$),[158,159] where α increases as the amount of Ni^{2+} increases ($\alpha \approx 0$ at $y \leq 0.07$, $\alpha = 0.02$ at $y = 0.25$).[159] The cation disorder has important consequences for Li^+ transport. The presence of Ni^{2+} in the interlayer Li^+ sites induces local reduction of spacing between the transition-metal layers because the Ni^{2+} is oxidized into the smaller Ni^{3+} cation during charge. That results in blocked Li ion diffusion and irreversible capacity loss on the first cycle.[160] Furthermore, the position of the $Ni^{3+/4+}$ couple in $LiNiO_2$ can result in preferential oxidation of the lattice oxide ions and hence evolution of O_2 on charging of the electrode, with concomitant safety issues. Therefore, Ni^{3+} substitution by Co^{3+} was examined in order to stabilize the oxidation state and reduce Ni^{2+} formation. Within the wide range of $Li[Ni_{1-x}Co_x]O_2$ materials, in particular $LiCo_{0.3}$-$Ni_{0.7}O_2$ shows a lower irreversible capacity[161] because of lower $Ni^{2+} \leftrightarrow Li^+$ site exchange[162,163] as well as better structural stability at high temperature.[164] The stability is further improved by Al (and other metal) doping, and hence $Li[Ni_{0.8}Co_{0.15}Al_{0.05}]O_2$ has seen tremendous commercial success. In addition, anion doping with F^- and S^{2-} on the O^{2-} sites[165,166] improves cycling performance as a result of reduced Ni migration into the Li layer. The phase transformations exhibited on (de)lithiation of Li_xNiO_2 are as complicated as those of $LiCoO_2$. They can be summarized as consisting of three single-phase reactions and three two-phase reactions: (H1 $(0 < x < 0.15) \leftrightarrow$ H1 + M $(0.15 < x < 0.25) \leftrightarrow$ M $(0.25 < x < 0.5) \leftrightarrow$ M + H2 $(0.5 < x < 0.57) \leftrightarrow$ H2 $(0.57 < x < 0.68) \leftrightarrow$ H2 + H3 $(0.68 < x)$, H: hexagonal, M: monoclinic phase).[167,168]

$LiMnO_2$. Layered $LiMnO_2$ is a very attractive material from an economical and environmental point of view. However, its thermodynamically stable form is a poorly electrochemically active orthorhombic structure that is different from the ($R\bar{3}m$) phase.[169] Therefore, formation of layered $LiMnO_2$ is not possible via conventional solid state synthesis methods used to make the layered Co or Ni analogues. Ion exchange of thermodynamically stable layered $NaMnO_2$ with Li^+ is necessary to prepare the desired metastable phase, as independently reported by Bruce et al.[170] and Delmas et al.[171] Layered $LiMnO_2$ exhibits a small monoclinic ($C2/m$) deformation of the ideal rhombohedral structure due to Jahn−Teller distortion of Mn^{3+}. Nonetheless, on cycling, layered $Li_{0.5}MnO_2$ converts into the $LiMn_2O_4$ spinel structure[172] because the latter is more stable,[173] resulting in poor electrochemical properties and a spinel-like drop in the voltage profile. This conversion from layered to spinel-like structure is facilitated owing to the same cubic-close-packed (ccp) sublattice of oxygen ions adopted by layered $LiMnO_2$ and spinel $LiMn_2O_4$ phases. Conversion requires only cation diffusion. Even Co doping in layered $LiMnO_2$ cannot prevent this transition, though it does enhance the electrochemical performance.[174] In an effort to inhibit the transformation, a layered lithium manganese oxide with the so-called O2 structure, $Li_{2/3}[Li_{1/6}Mn_{5/6}]O_2$, which exhibits a different oxygen sublattice from O3 $LiMnO_2$ was prepared by Dahn et al. via ion exchange from P2 $NaMnO_2$.[175] As the O2 (and P2) structures comprise a very different oxygen lattice, transition into the spinel is prohibited at room temperature since it would require rearrangement of the lattice via oxygen diffusion. Unfortunately, the electrochemical performance of $Li_{2/3}[Li_{1/6}$-$Mn_{5/6}]O_2$ is compromised because of poor crystallinity because of stacking faults. Partial substitution of Mn with Ni[176] and Co[175] is successful in achieving somewhat better electrochemical behavior.

$LiMn_{0.5}Ni_{0.5}O_2$. The above studies led to solid-solution approaches to $LiMO_2$ (M = Ni, Mn, Co, etc/) that could be considered as compensating one metal's disadvantage with another's advantage. The $LiNi_{1-x}Mn_xO_2$ $(x \leq 0.5)$ system was first reported in 1992 by Dahn et al.,[177] but it did not receive much attention because of poor electrochemical behavior. This system was revisited by Ohzuku et al. ($LiNi_{0.5}Mn_{0.5}O_2$)[178] and Dahn et al. ($Li[Ni_x$-$Li_{(1/3-2x/3)}Mn_{(2/3-x/3)}]O_2$)[179] in 2001. They demonstrated greatly improved electrochemical performance of Li-$Ni_{0.5}Mn_{0.5}O_2$, related to the heating temperature (>800 °C) employed in the synthesis. Similar results were obtained for the analogous and even more promising $LiCo_{1/3}Ni_{1/3}Mn_{1/3}O_2$ material[180] (see next section). Reversible capacities exhibited by $LiNi_{0.5}Mn_{0.5}O_2$ obtained by reacting LiOH and nickel manganese double hydroxides at 1000 °C in air were reported to be 200 mA h g^{-1} (2.5−4.5 V window vs. Li/Li^+) with little capacity fading (Figure 16).[181] Other advantages of $LiNi_{0.5}Mn_{0.5}O_2$ are lower thermal runaway, better structural thermal stability than $LiCoO_2$ or $LiNiO_2$, and greater inhibition to reaction with electrolytes in the charged state.[181,182] Cycled

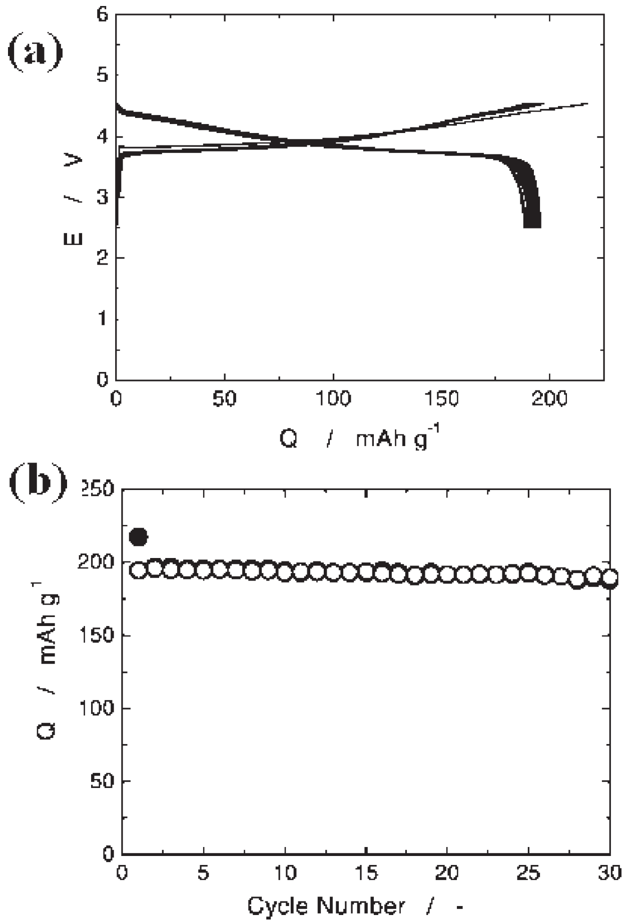

Figure 16. (a) Charge and discharge curves of a Li/$LiNi_{1/2}Mn_{1/2}O_2$ cell operated in voltages of 2.5−4.5 V at a rate of 0.17 mA cm^{-2} for 30 cycles. (b) Charge and discharge capacities as a function of cycle number for a cell operated in voltages of 2.5−4.5 V as shown in a. Closed and open circles indicate charge and discharge capacities, respectively. Reprinted from reference 181, Copyright 2003, with permission from Elsevier.

$Li_xNi_{0.5}Mn_{0.5}O_2$ ($x = 0.2, 0.9$) also shows a higher onset temperature of oxygen release and reduced oxygen loss compared to $Li_{0.3}NiO_2$ and $Li_{0.3}Ni_{0.7}Co_{0.15}Al_{0.15}O_2$ as a result of increased structural stability.[183]

There are two ways that the valence states of the metal can be accommodated in $LiNi_{0.5}Mn_{0.5}O_2$: as Ni^{3+} and Mn^{3+} as originally thought,[184] or as Ni^{2+} and Mn^{4+} as speculated[185] and proven by X-ray adsorption spectroscopy[42] and first principles calculations.[186] Only the Ni participates in the redox behavior, undergoing a reversible change between +2 and +4 in the range of $0 < x < 1$ (ca. 4.0 V vs. Li/Li^+). However, it has been proposed that most charge compensation actually occurs at hybridized 2p-like levels with local weight near the oxygen atoms.[187] The “formally invariant” valence state of Mn^{4+} in the range of $0 < x < 1$ accounts for some of the stability of the material upon cycling;[42] i.e, $Li_{1-x}Ni_{0.5}Mn_{0.5}O_2$ is free from either a transition into a spinel-like phase or any Jahn−Teller distortion of Mn^{3+} during charge and discharge. The redox potential of $Li_xNi_{0.5}Mn_{0.5}O_2$ is very similar to that of Li_xNiO_2, although it should be lower because of the greater span of oxidation states. This contradiction is explained by two theoretical models. One concludes that the energy difference in the attractive interaction (mixing) between Ni and Mn at $x = 1$ and the repulsive interaction between them at $x = 0$ in $Li_xNi_{0.5}Mn_{0.5}O_2$ can raise the potential by 226 mV compared to the pure Ni host.[186] The other assumes that Mn and O contribute ∼10% and ∼5%, respectively, for charge compensation in the range of $0 < x < 1$ of $Li_xNi_{0.5}Mn_{0.5}O_2$, which reflects the covalent mixing in the system. Therefore, Mn may not be completely inert.[188]

$LiNi_{0.5}Mn_{0.5}O_2$ possesses the classic α-$NaFeO_2$ ($R\bar{3}m$) structure, with 8−10% cation disorder between the 3a and 3b sites due to the similar size of Ni^{2+} and Li^+ (as discussed above). This cation disorder impedes the kinetics of Li diffusion as described above for $LiNiO_2$.[178] The effect of disorder on Li ion diffusivity in layered transition metal oxides can be explained in various ways.[189,190] The site-exchanged transition metal (M) ions within the Li slabs (i) disrupt the lithium-ion diffusion path, (ii) increase electrostatic repulsion between M and Li, resulting in a lower Li mobility, and (iii) reduce the Li slab space, resulting in a higher activation barrier to lithium diffusion. Li diffusivity in the layered metal oxides takes place by migration through a tetrahedral site (octahedral−tetrahedral−octahedral). The size of this site is determined by the *c*-lattice parameter (Li slab space). Therefore, the high reversible capacity (200 mA h g^{-1}) of $LiNi_{0.5}Mn_{0.5}O_2$ is achieved only at slow current densities (0.17 mA cm^{-2}).[181] To solve the problem of cation disorder in $LiNi_{0.5}Mn_{0.5}O_2$, we introduced three different strategies. In 2006, Kang et al.[191] decreased the amount of cation disorder to 4.3% by preparing the material via ion exchange from $NaMn_{0.5}Ni_{0.5}O_2$. The latter exhibits no disorder because of the larger size difference between Na^+ ($r_{Na+} = 1.02$ Å) and Ni^{2+} ($r_{Ni2+} = 0.69$ Å), Mn^{4+} ($r_{Mn4+} = 0.53$ Å). This material exhibits vastly improved rate capability, delivering 183 mA h g^{-1} at a 6*C* rate (1*C* rate: 280 mA g^{-1}). In 2006, Schougaard et al.[192] also reduced the nickel content in the lithium layer to 5.6% by adjusting the stoichiometry to $LiNi_{0.5+\delta}Mn_{0.5-\delta}O_2$. At $\delta = 0.06$, this results in an equivalent partial substitution of 0.06 Ni^{3+} for Ni^{2+} for charge compensation. It was proposed that better cation ordering is induced because the elastic energy related to the different ionic sizes can overcome the entropy associated with cation disorder.[193] Better rate performance was demonstrated as a result (ca. 110 mA h g^{-1} at 4*C*). Finally, Breger et al.[194] showed that Ni in the Li layers can be electrochemically induced to migrate to the transition metal layers. From combined neutron diffraction/^{6}Li MAS NMR/electrochemistry studies and first principle calculations, they prove that Ni migrates from the Li layer to transition metal (TM) sites vacated by Li at > 4.6 V vs. Li/Li^+ (the octahedral Li in TM sites is electrochemically extractable).[195] Therefore, charging to high voltage (5.3 V vs Li/Li^+) can reduce the cation disorder. This results in better electrochemical performances on subsequent cycling within the voltage range of 2.0−4.5 V vs Li/Li^+, compared to an electrode that had not undergone charging to high voltage.,[196]

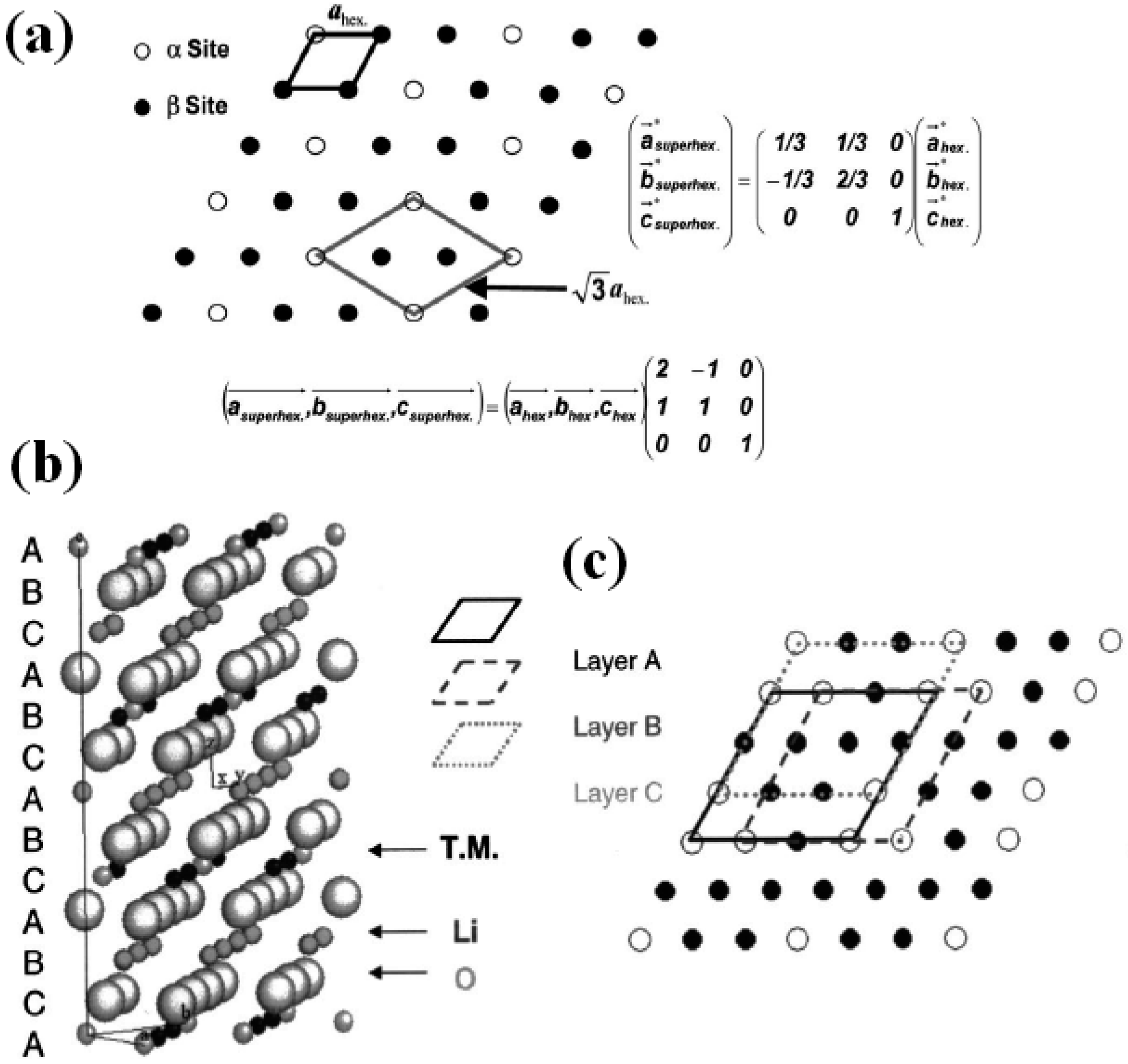

Figure 17. (a) Schematic of in-plane cation ordering in the transition-metal layer in $LiNi_{0.5}Mn_{0.5}O_2$. Multiplicity of α and β are 1/3 and 2/3, respectively, in a triangular lattice plane. The transformation matrix of the $\sqrt{3}a_{hex} \times \sqrt{3}a_{hex} \times c_{hex}$ superstructure with respect to the parent hexagonal cell is presented. (b) Proposed structure of $LiNi_{0.5}Mn_{0.5}O_2$ with $P3_112$ space group. (c) $[001]_{hex}$ projection of transition metal layers reveals 3-fold screw axis along the *c* axis. Reproduced with permission from reference 199. Copyright 2004, The Electrochemical Society.

Because of the structural complexity of $Li_xMn_{0.5}Ni_{0.5}O_2$ associated with cation disorder, numerous debates have existed regarding its detailed structure and phase transformations on (de)lithiation.

(i) Structure: On the basis of XRD, Lu et al. reported that compositions $Li[Ni_xLi_{(1/3-2x/3)}Mn_{(2/3-x/3)}]O_2$ are solid solutions for $x < 1/2$.[179] The material exhibits superlattice ordering of the Li, Ni, and Mn atoms in the transition metal layers at $x < 1/3$ as predicted, but not for $x = 1/2$. The formation of local domains of Li_2MnO_3 was not indicated.[179,197] On the basis of ^6Li MAS NMR results, Yoon et al. also provided data to support short-range ordering. Their results indicate that Li in the transition metal layers is surrounded by 6 Mn^{4+} ions in the first cation coordination sphere, $Li(OMn)_6$.[42,198] Conversely, data from Meng et al.[199] showed unique superstructure reflections of $LiMn_{0.5}Ni_{0.5}O_2$ ($x = 1/2$ in $Li[Ni_xLi_{(1/3-2x/3)}Mn_{(2/3-x/3)}]O_2$). TEM analysis suggested the formation of a $\sqrt{3}a_{hex} \times \sqrt{3}a_{hex} \times c_{hex}$ superstructure (Figure 17a), implying long-range ordering in the transition metal layer that led them to propose a $P3_112$ superstructure (Figure 17b and c). The short-range ordering of $LiMn_{0.5}Ni_{0.5}O_2$ is consistent with its magnetic properties,[200] and is bolstered by theoretical models from first principle calculations,[201,202] such as the zigzag model for ion-exchanged samples[203] and the flower-cluster model for high-temperature samples.[204] Overall, the cation ordering behavior in $LiMn_{0.5}Ni_{0.5}O_2$ is undoubtedly associated with the synthesis temperature and heating/cooling history, which can lead to discrepancy in the experimental observations.[205]

(ii) Phase transformations: Yang et al.[206] reported that $LiMn_{0.5}Ni_{0.5}O_2$ undergoes a phase transition between two hexagonal structures (H1 $\leftrightarrow$ H2) on delithiation which is reversible on cycling. This is in contrast to studies based on chemical delithiation, where Venkatraman et al.[207] reported that $Li_xMn_{0.5}Ni_{0.5}O_2$ experiences a simple single-phase reaction in the full range of $0 \leq x \leq 1$. Arachi et al. reported that a monoclinic ($C2/m$) phase of $Li_xMn_{0.5}Ni_{0.5}O_2$ is formed at $x = 0.5$[208] and $0.7 < x < 0.8$.[209]

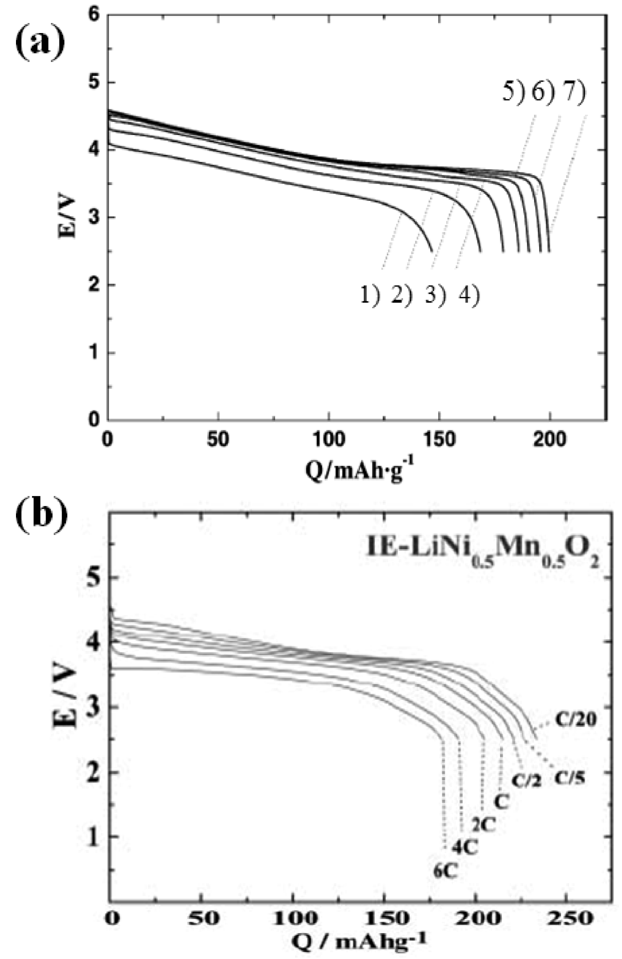

Figure 18. Discharge rate capability of (a) $LiCo_{1/3}Ni_{1/3}Mn_{1/3}O_2$ and (b) $LiMn_{0.5}Ni_{0.5}O_2$. (a) The cell was charged at 0.17 mA cm^{-2} up to 4.6 V and then discharged to 2.5 V at (1) 1600, (2) 800, (3) 400, (4) 200, (5) 100, (6) 50, and (7) 18.3 mA g^{-1}. (b) The cell was charged at C/20 to 4.6 V, then held at 4.6 V for 5 h and discharged at different rates. 1C corresponds to 280 mA g^{-1}. Figure a reprinted from reference 222, Copyright 2003, with permission from Elsevier. Figure b reproduced from reference 191. Reprinted with permission from AAAS.

Finally, complete delithiation to $Ni_{0.5}Mn_{0.5}O_2$ on charging to 5.3 V vs. Li/Li$^+$ results in conversion of the O3 to the O1 phase, similar to the case of $LiNiO_2$.[196]

$LiCo_{1/3}Ni_{1/3}Mn_{1/3}O_2$. The metals Co, Ni, and Mn can all be accommodated in the layered metal oxide structure, to give a range of compositions $Li[Co_xNi_yMn_z]O_2$ ($x + y + z = 1$). One composition, $LiCo_{1/3}Ni_{1/3}Mn_{1/3}O_2$ reported in 2001 by Ohzuku et al., has shown particularly promising electrochemistry and intriguing structural behavior. It possesses the same α-$NaFeO_2$-type structure as $LiMn_{0.5}Ni_{0.5}O_2$,[180] with Ni, Co, and Mn adopting valence states of 2+, 3+, and 4+, respectively.[210,211] It can be considered as a 1:1:1 solid solution of $LiCoO_2$, $LiNiO_2$, and $LiMnO_2$[202] or a 1:2 solid solution between $LiCoO_2$ and $LiNi_{0.5}Mn_{0.5}O_2$ (i.e., $LiCo_{1-2x}Ni_xMn_xO_2$).[212] Co-doping of $LiMn_{0.5}Ni_{0.5}O_2$ benefits a highly ordered structure. The degree of cation disorder (1−6%)[213−218] in $LiCo_{1/3}Ni_{1/3}Mn_{1/3}O_2$ is less than that of $LiMn_{0.5}Ni_{0.5}O_2$ (8−10%), which was clearly observed in previous studies of $LiCo_yMn_{0.2}Ni_{0.8-y}O_2$ (cation disorder: 7.2% at $y = 0$ and 2.4% at $y = 0.3$).[219] In addition, $Li_{1-x}Co_{1/3}Ni_{1/3}Mn_{1/3}O_2$ only exhibits a 1−2% volume change in the range of $0 < x \lesssim 0.7$.[213,216,220,221] Thus, not only does a low amount of cation disorder contribute to its excellent electrochemical performance but the small volume change is also important. The material shows good rate capability (200 mA h g^{-1} at 18.3 mA g^{-1} and 150 mA h g^{-1} at 1600 mA g^{-1})[222] similar to ion-exchanged $LiMn_{0.5}Ni_{0.5}O_2$ (183 mA h g^{-1} at 1680 mA g^{-1}), as shown in Figure 18.[191] Another attractive property of $LiCo_{1/3}Ni_{1/3}Mn_{1/3}O_2$ is its excellent safety properties at a high state of charge, compared to $LiNiO_2$, $LiCoO_2$, and $LiNi_{0.8}Co_{0.15}Al_{0.05}O_2$.[222,223]

Similar to the case of $LiMn_{0.5}Ni_{0.5}O_2$, much effort has been expended on $LiCo_{1/3}Ni_{1/3}Mn_{1/3}O_2$ to clarify the mechanism of charge compensation during charge and discharge. On the basis of the combined NMR and soft and hard X-ray absorption spectroscopy (XAS) studies, Yoon et al.[224,225] reported that the major charge compensation at the metal site on Li deintercalation is achieved by the oxidation of Ni^{2+} to Ni^{3+} (surface) and Ni^{4+} (bulk), while Co^{3+} and Mn^{4+} remain in their original valence states. They also report that a portion of the charge compensation during Li deintercalation is achieved in the oxygen site associated with the presence of Co. This explanation is consistent with XAS results reported by Tsai et al.,[226] but not with earlier results of Miao et al.[187] They claimed that charge compensation is primarily associated with oxygen, but not Ni, Mn, and Co. In contrast, Hwang et al. used a combined computational/experimental (XANES) study to show that the redox couples in $Li_{1-x}Co_{1/3}Ni_{1/3}Mn_{1/3}O_2$ are Ni^{2+}/Ni^{3+}, Ni^{3+}/Ni^{4+}, and Co^{3+}/Co^{4+}, in the range of $0 \le x \le 1/3$, $1/3 \le x \le 2/3$, and $2/3 \le x \le 1$, respectively.[211] This result is in agreement with a theoretical model by Koyama et al.[210] XAS data reported by Kim et al.[216] indicated that the Ni^{2+}/Ni^{4+} redox couple is near 3.75 V and the Co^{3+}/Co^{4+} couple occurs over the entire range of charge/discharge.

Additional debate is associated with the reaction mechanism of $LiCo_{1/3}Ni_{1/3}Mn_{1/3}O_2$. Results reported by Choi et al.[221] indicated that $Li_{1-x}Co_{1/3}Ni_{1/3}Mn_{1/3}O_2$ is chemically stable as the O3 structure type without the loss of any oxygen from the lattice at $(1-x) > 0.35$. This was supported by X-ray and neutron diffraction studies of Yin et al.[213] who showed that $Li_{1-x}Co_{1/3}Ni_{1/3}Mn_{1/3}O_2$ undergoes a phase transition from the starting O3 phase ($R\bar{3}m$) to the O1 phase of $Li_{0.04}Co_{1/3}Ni_{1/3}Mn_{1/3}O_2$ ($P\bar{3}m1$) at $(1-x) = 0.3$ without oxygen loss. However, Yabuuchi et al.[220] and Kim et al.[216] claimed that they could not observe any phase associated with O1 stacking.

The structure of $LiCo_{1/3}Ni_{1/3}Mn_{1/3}O_2$ was originally proposed to be a [$\sqrt{3} \times \sqrt{3}$] R30°-type superlattice structure with long-range ordering based on first-principle calculations when it was introduced by Ohzuku et al.[180,210] On the basis of subsequent electron diffraction, XRD, and XAS studies, the same group suggested that this superlattice adopted a $P\bar{3}12$ space group.[227] Local ordering within the transition metal layers was supported by other studies, but further evidence for the long-range $LiCo_{1/3}Ni_{1/3}Mn_{1/3}O_2$ superstructure remains elusive. Diffraction data were reported to be consistent with a random distribution of Mn, Ni, Co in the 3a site.[215] Cahill et al.[218] showed evidence of local ordering driven by local charge balance (Pauling's electroneutrality) related to Ni^{2+}-Mn^{4+} association using solid state ^6Li NMR. Their NMR result is consistent with another NMR study obtained by Zeng et al.[228] The latter also observed a tendency for the formation of Ni^{2+} and Mn^{4+} clusters within the transition metal layers. In addition, short-range ordering is supported by data obtained from electron paramagnetic resonance (EPR) spectroscopy[229] and XAS.[226]

$xLi_2MnO_3\cdot(1-x)LiMO_2$. Another promising lithium metal oxide cathode material is $xLi_2MnO_3\cdot(1-x)LiMO_2$, referred to as a composite (or integrated) structure.[230] It is based on Li_2MnO_3, a layered monoclinic, $C2/m$ structure with cation ordering. This structure can be formulated as $Li[Li_{1/3}Mn_{2/3}]O_2$ composed of alternating Li layers and Li+Mn (1:2) layers. The $LiMO_2$ component can comprise $LiMn_2O_4$ (spinel)[231] or more generally layered oxides such as $LiMn_{0.5}Ni_{0.5}O_2$[232] and $LiCo_{1/3}Ni_{1/3}Mn_{1/3}O_2$,[233] as described in recent reviews. The most attractive property of the composite electrode is its high reversible capacity (ca. 200−300 mA h g^{-1}) following an "activation" process. The $xLi_2MnO_3\cdot(1-x)LiMO_2$ composite electrode was originally designed to structurally stabilize $LiMnO_2$ with Li_2MnO_3 since the latter is electrochemically inactive between 3 and 4 V vs. Li/Li^+.[234] However, Li_2MnO_3 can transform into an active phase, $Li_{2-x}MnO_{3-(x/2)}$ (MnO_2 at $x = 2$) by the leaching of Li_2O via chemical and electrochemical means. Thackeray et al. showed that Li_2MnO_3 ($C2/m$) decomposes into $Li_{0.27}[Mn_{0.91}Li_{0.09}]O_2$ by acid treatment; $Li[Mn_{0.91}Li_{0.09}]O_2$ ($R\bar{3}m$) is then formed by relithiation.[235,236] Kalyani et al. report that Li_2MnO_3 can be activated electrochemically by charging at 4.5 V vs. Li/Li^+. Both Li_2MnO_3 materials show a reversible capacity of ca. 200 mA h g^{-1}, but electrochemical activation induces higher irreversible capacity associated with leaching of Li_2O.[237]

As earlier described (vide supra) the compositions $xLi_2MnO_3\cdot(1-x)LiMn_{0.5}Ni_{0.5}O_2$ were first described by Dahn et al. as a solid solution, namely as $Li[Ni_yLi_{(1/3-2y/3)}Mn_{(2/3-y/3)}O_2$ $(0 < y < 0.5)$.[179,238] Work by Thackeray et al. proposes that the composition be considered as a composite or "integrated" structure composed of nanodomains with two different phases (or different local structure) of layered Li_2MnO_3 and layered $LiMn_{0.5}Ni_{0.5}O_2$. The latter claims are based on the existence of Li_2MnO_3 nanodomains in the composite electrode of $xLi_2MnO_3.(1-x)LiMn_{0.5}Ni_{0.5}O_2$ as demonstrated by XRD reflections associated with a Li_2MnO_3 superlattice; by NMR spectra that indicate a Li_2MnO_3-like cation ordering, and quantitative TEM analysis that show an inhomogeneous structure.[232] This composite structure is more evident in the case of the layered-spinel ("splayered") composite structure of $xLi_2MnO_3\cdot(1-x)Li_{1+y}Mn_{2-y}O_4$ $(0 < x < 1, 0 \leq y \leq 1/3)$. Johnson et al. reports the high-resolution TEM image of $0.7Li_2MnO_3\cdot0.3Li_4Mn_5O_{12}$ that show the integrated structure of layered (Li_2MnO_3 (001) fringes) and spinel ($Li_4Mn_5O_{12}$ (111) fringes) nanosized domains, as shown in Figure 19.[231]

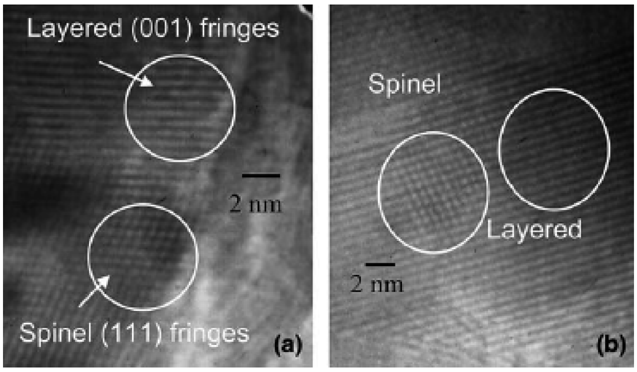

Figure 19. (a ,b) High-resolution TEM images of $0.7Li_2MnO_3\cdot0.3Li_4Mn_5O_{12}$ showing the structural compatibility of layered (Li_2MnO_3) and spinel ($Li_4Mn_5O_{12}$) domains. Reprinted from reference 231, Copyright 2005, with permission from Elsevier.

As mentioned above, the $xLi_2MnO_3\cdot(1-x)LiMO_2$ composite materials exhibit high reversible capacities after the activation process. During charging at 4.5 V vs. Li/Li^+, Ni^{2+} is oxidized into Ni^{4+}, and then Li_2O is extracted from Li_2MnO_3 above 4.5 V, to result in $xMnO_2\cdot(1-x)Mn_{0.5}Ni_{0.5}O_2$.[239] Li_2O extraction from the structure ($Li[Ni_{0.2}Li_{0.2}Mn_{0.6}]O_2$) has been directly confirmed by oxygen gas detection using in situ differential electrochemical mass spectroscopy (DEMS).[240] Recently, Li_2O extraction is also suggested to be related to electrolyte decomposition accompanied by a change in the Ni oxidation state.[241] Without the electrochemical activation of $0.3Li_2MnO_3\cdot0.7LiMn_{0.5}Ni_{0.5}O_2$[239] above 4.5 V, reversible charge capacities are on the order of 168 mA h g^{-1} (similar to theoretical charge capacity of $0.7LiMn_{0.5}Ni_{0.5}O_2$ = 184 mA h g^{-1}). After electrochemical activation, the reversible discharge capacity delivers 287 mA h g^{-1}. This is actually higher than the theoretical value of 262 mA h g^{-1} (184 mA h g^{-1} corresponding to $0.7(Ni^{2+}\leftrightarrow Ni^{4+})$ + 79 mA h g^{-1} by $0.3MnO_2$ obtained from $0.3Li_2MnO_3$). The anomalously higher capacity of the composite electrodes compared to the theoretical is especially observed for $xLi_2MnO_3\cdot(1-x)LiCo_{1/3}Ni_{1/3}Mn_{1/3}O_2$ at high temperature (50 °C).[242] Formulating these mixed compositions as $xA\cdot(1-x)B$, after electrochemical activation the discharge capacities of $0.7A\cdot0.3B$, $0.5A\cdot0.5B$, and $0.3A\cdot0.7B$ are 311, 286, and 287 mA h g^{-1}, respectively, in contrast to their theoretical discharge capacities of 242, 251, and 262 mA h g^{-1}. The theoretical value is calculated based on the xLi that can be de/inserted in $xMnO_2$ obtained from xLi_2MnO_3 ("A") and also the $(1-x)$Li that can be de/inserted in $(1-x)LiMO_2$ ("B"). The reason for the anomalous capacity of the composite electrodes is not clear. It has also recently been reported that the rate capabilities of these composite electrodes are highly enhanced by coating them with $LiNiPO_4$, although the underlying mechanism needs further investigation.[243]

4. Positive Electrodes for Li–Sulfur and Li–Air Cells

Following two decades of optimization, batteries based on intercalation chemistry are approaching the energy density limits provided by topotactic redox reactions. They are now experiencing commercial success beyond the powering of portable electronic devices and power tools–for example, they are being employed in upcoming first-generation plug-in hybrid electric vehicles (PHEV). Electric vehicles (EV's) based on these batteries such as the Tesla Roadster are already in the marketplace, and many others have been developed that are aimed for introduction within the next year. But to extend the driving range of PHEV's and EV's, and reduce cost factors, new systems with substantially higher energy density are being sought for the next-generation batteries, that move beyond intercalation chemistry into the realm of "integration" chemistry. These batteries would also be suitable for other types of large-scale energy storage systems coupled to renewable energy sources.

Li–S cells. The low equivalent weight, low cost, high capacity, and environmental friendliness of sulfur identify it as a very suitable positive electrode material, thus motivating considerable investigation over the past decade. The sulfur electrode operates quite differently to the insertion electrodes described above. As opposed to the intercalation of Li^+/e^- into a host structure with minor perturbation to the framework, the reduction of sulfur involves a reversible chemical reaction with lithium to form another material. We call this an "integration" reaction. Extensive studies have shown that this occurs via a redox cascade of intermediate "molecular" polysulfides (in order of decreasing sulfur oxidation state: $Li_2S_8 \leftrightarrow Li_2S_6 \leftrightarrow Li_2S_5 \leftrightarrow Li_2S_4$), followed by the formation of insoluble Li_2S_2 and finally Li_2S.[244,245] The overall redox couple, described by the reaction $S_8 + 16Li \leftrightarrow 8Li_2S$, lies at an average of about 2.1 V with respect to $Li^+/Li°$. The potential is about 2/3 of that exhibited by conventional positive electrodes, but this is offset by the very high theoretical capacity afforded by the nontopotactic integration process, of 1675 mA h/g. Thus, compared to conventional batteries, Li–S batteries have the opportunity to provide a gravimetric energy density that is a factor of at least 3–5 times higher. Theoretical values can approach 2500 W h/kg or 2800 W h/L on a weight or volume basis, respectively,[246,247] assuming complete reaction to Li_2S. The kinetics of the reactions on the high oxidation state side between $S^0 \leftrightarrow S^{0.5-}$ are fast (i.e., conversion of S_8 through the sequence of soluble molecular polysulfides to form S_4^{2-}) compared to those of the lower oxidation states. Reaction of $S^{0.5-} \leftrightarrow S^{1-}$ to form insoluble Li_2S_2 is somewhat hindered owing to the energy required for nucleation of the solid state phase, and the interconversion of Li_2S_2 to Li_2S is impeded due to the sluggishness of solid-state diffusion in the bulk. The reaction sequence on reduction and oxidation and the corresponding electrochemical profile is depicted in Figure 20.

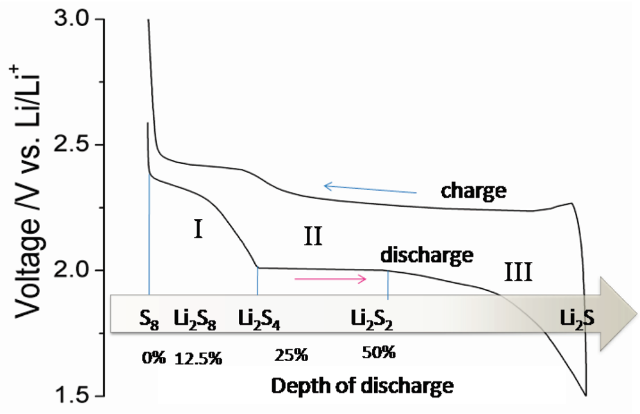

Figure 20. Discharge–charge profile of a Li–S cell, illustrating: (I) conversion of solid sulfur to soluble polysulfides; (II) conversion of polysulfides to solid Li_2S_2; (III) conversion of solid Li_2S_2 to solid Li_2S.

Despite the considerable advantages of the Li–S cell, it is plagued with problems that have prevented its practical realization until recently. One is the very poor electronic conductivity of sulfur and its discharge product (Li_2S_2/Li_2S), which necessitates contact with substantial fractions of conductive species such as carbon or metals. Early configurations of the sulfur electrode consisted of simple mixtures of sulfur and carbon particles.[248,249] These cells suffered low capacity, and poor discharge/cycle efficiency. Much attention has been devoted to increasing the conductivity of the sulfur electrode. Composites with sulfur embedded within a conducting polymer have shown some promise.[250] However, the large polarization exhibited by these materials reduces the energy density. The low surface area of the conducting polymer also limits the loading of sulfur active mass. The conductivity of the sulfur electrode can be better enhanced by contact with carbonaceous materials on a more intimate level, such as that afforded by MWCNT's.[251] Reversible capacities of up to 700 mA/g were reported, but capacity fading is an issue and contact is not optimum.

Another major challenge arises from the solubility of the polysulfide ions (S_n^{2-}) formed on reduction of S_8 or upon oxidation of Li_2S,[252] which escape from the sulfur electrode and enter the electrolyte. They diffuse to the lithium negative electrode where they react directly with lithium in a parasitic reaction to create lower order polysulfides. These species diffuse back to the positive electrode and are reoxidized into the original higher order polysulfides. The above process takes place repeatedly, thus creating an internal "shuttle" phenomenon, which markedly reduces the Coulombic efficiency. Some irreversibility of the process also causes the build-up of impedance layers on both electrodes. Self-discharge of the polysulfides onto the Li anode on the completion of each discharge cycle results in some fraction being subjected to deep reduction to solid Li_2S_2 and/or Li_2S. These materials gradually form a thick layer on the anode surface over prolonged cycling,[253] and become electrochemically inaccessible and causes active mass loss and capacity fading. Deposition on the positive electrode can also occur. This blocks ionic pathways into the inner parts of the sulfur electrode and impedes further electrochemical reactions. Mathematical modeling has yielded a good quantitative analysis of the shuttle phenomenon in Li/S rechargeable batteries.[254] It encompasses theoretical models of the charge process, charge and discharge capacity, overcharge protection, thermal effects, self-discharge, and a comparison of simulated and experimental data. The study provides evidence that self-discharge, charge−discharge efficiency, and overcharge protection are all facets of the same phenomenon.

One approach for Li−S batteries are "all liquid" systems[244] that rely on dissolution of the polysulfides in the electrolyte. Although the ionic conductivity of these "catholyte" cells is very high, the volumetric capacity is quite low because of the large volumes of electrolyte required. Electrolyte additives are also beneficial to maintain solubility and increase the fraction of active species in solution.[255] Most importantly, unless reduction of the polysulfides on the metallic Li anode is inhibited, rapid capacity fading ensues. Anode membranes that permit Li-ion transport to and from the metallic Li surface and provide a critical protective layer have been developed by PolyPlus.[256] Visco et al. have also proposed coating the cathode with a mixed ionic electronic conductor (MIEC).[257] They claim that the MIEC layer allows rapid removal of discharge product precipitates on the cathode.

Extensive work has also been carried out to prevent polysulfide dissolution. Ahn et al. reported that $Mg_{0.6}Ni_{0.4}O$ particles (~50 nm) as a cathode additive exhibit some degree of adsorption for polysulfide ions.[258] Gorkovenko et al. describes that porous carbon materials can retard the polysulfide dissolution.[259] Polymer electrolytes have also been used. The first "all solid" cell system employing a gel-like polymer electrolyte was described long ago.[246] However, this cell achieved practical discharge efficiency only at high temperatures (above 80 °C), and it suffered capacity fading over cycling.[260] More recently, Cairns and co-workers have investigated rechargeable Li/S cells containing a variety of polymer-containing electrolytes, including polyethylene oxide (PEO),[261] polyethylene glycol-dimethyl ether (PEGDME),[262] and mixtures of PEGDME or tetraethylene glycol-dimethyl ether (TEGDME) with ionic liquids.[263,264] First discharge capacities at slow rates are more than 1400 mA h/g S, but the initial capacity fade on cycling is rapid. After 300 cycles, the specific capacity is above 200 mA h/g S for electrodes containing 70% S. With the ionic liquid containing electrolytes, specific capacities of more than 250 mA h/g S are obtained at 0 °C after 20 cycles, and 700 mA h/g S at 25 °C after 10 cycles. The maximum cycle life reported is 565 cycles, with gradual capacity loss. The lithium metal electrodes showed no sign of dendrites or shorting after several hundred cycles. The use of polymer-based electrolytes avoids volatile organic solvents, leading to significantly improved safety. However, these solutions still fall short of the mark for stable long-term electrochemical performance.

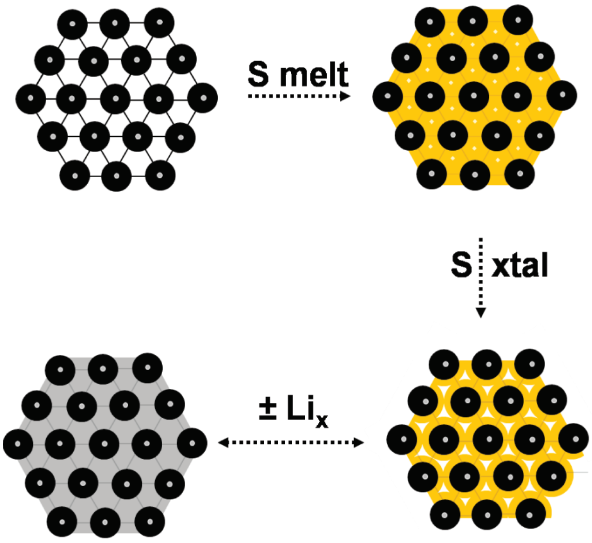

Figure 21. Schematic of the sulfur (yellow) confined in the interconnected pore structure of mesoporous carbon, CMK-3, formed from carbon tubes that are propped apart by carbon nanofibers to form channels. The view is down the channels and tubes in cross-section. The lower scheme represents the subsequent discharging−charging of sulfur with Li, illustrating the strategy of pore filling to tune for volume-expansion/contraction. Reprinted by permission from Macmillan Publishers Ltd. from reference 265, copyright 2009.

To date, the best electrochemical properties that have been reported for "contained" sulfur systems are exhibited by ordered interwoven carbon/sulfur composites that comprise high pore-volume carbons with 1D or 3D channel nanostructures.[265] Sulfur is readily incorporated from the melt by capillary forces and shrinks upon solidification to provide open pathways for electrolyte/Li^+ ingress. The conductive carbon framework constrains the sulfur within its channels and generates essential electrical contact as shown schematically in Figure 21. Kinetic inhibition to diffusion within the framework and the sorption properties of the carbon aid in trapping the polysulfides formed during redox. Thus immobilized, full reduction to Li_2S_2/Li_2S (or oxidation to S_8 on charge) is achieved within the carbon framework. Polymer modification of the carbon surface further provides a chemical gradient that retards diffusion of these large anions out of the electrode, facilitating a more complete reaction. Reversible capacities up to 1320 mA h/g are attained with no overcharge and 99.9% efficiency on the first cycle, indicating the shuttle mechanism is totally suppressed. Capacity fading is reduced because of greatly reduced polysulfide concentration in the electrolyte, and the materials sustain reversible capacities of 1100 mA h/g.

Li−Air Cells. The Li−air cell is similar to Li−S in numerous ways. It also represents "integration" chemistry, but is based on the reaction of oxygen with lithium (see Figure 22). Although the reaction is limited to a one-electron reduction per oxygen atom to form Li_2O_2 as the product (i.e., $O_2 + 2Li+/2e^- \leftrightarrow Li_2O_2$), the average voltage is higher than Li−S and lies at a theoretical potential of about 3.0 V. The practical discharge potential is about 2.7 V. Li−air batteries have emerged as a potential alternative to Li−S, and have drawn significant

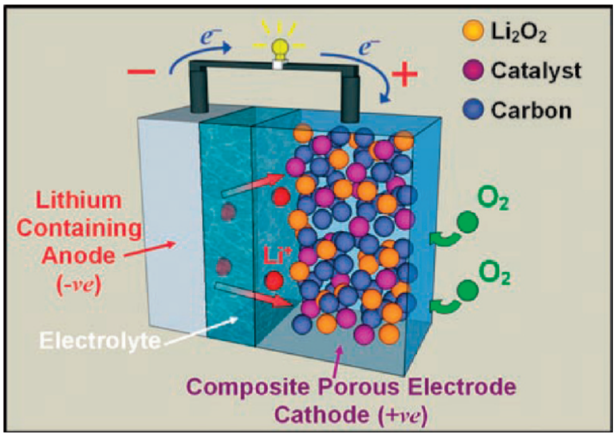

Figure 22. Schematic representation of a rechargeable Li/O_2 battery. Reproduced from reference 270 with permission. Copyright 2008 Wiley−VCH Verlag GmbH & Co. KGaA.

attention recently that highlights both their advantages and considerable challenges. The use of O_2 as the positive electrode is not a new concept. It is the basis for fuel cells, and zinc−air batteries (semifuel cells). These batteries rely on aqueous electrolytes which have a much narrower voltage "window", and a lower cell voltage. The first nonaqueous Li-air battery was reported by Abraham et al. in 1996,[266] but rechargeability was proven only recently by Bruce et al.[267] Li_2O_2 was determined to be the principle product after discharge, and O_2 was detected as the oxidation product on charge, confirming the reversibility of the reaction.

Similar to the case of the Li−S cell, the reaction at the positive electrode employs porous carbon and/or porous metal as the current delivery system for O_2 reduction[268] and as host for the product. The discharge reaction fills the voids with Li_2O_2 and terminates when these voids are filled. Unlike the Li−S battery, the intermediate superoxide, LiO_2, is not soluble and thus there is no possibility of an internal shuttle.[269] On the other hand, Li_2O_2 oxidation requires a (room-temperature) catalyst, and O_2 reduction benefits as well. The triple phase boundary, an omnipresent and limiting factor in fuel cells, governs reactivity. In the Li−air case, it is determined by the necessity of simultaneous contact of the electron delivery network; the reactants (O_2 and Li^+) via the electrolyte; and the catalyst necessary to carry out reduction and oxidation. Electrolytic manganese dioxide, and especially α-MnO_2 are reported to be among the most active catalysts[270] although other transition metal oxides such as Fe_2O_3, CuO, and Co_3O_4 also show much promise.[271] Nonetheless, high overpotentials are still observed along with substantial hysteresis on discharge−charge that is typically about 1.5 V. In the best data reported to date, the discharge potential is still 0.3−0.4 V below theoretical, and the charge potential is a full volt above. The problem of occlusion of the catalytic sites by formation of Li_2O_2 remains a serious challenge. On reduction, extensive nucleation of the product on the catalyst particle will block further catalytic activity and on oxidation, the lack of intimate contact of the Li_2O_2 with the catalyst can inhibit reactivity.

Similar to Li−S, catholyte systems in aqueous media have been investigated as a solution to the problems described above. They have drawbacks of reduced voltage and much lower volumetric capacity, but the advantage of a solubilized reaction product, LiOH,[272] eliminates some of the challenges of a confined cathode. However, such systems−much more so than the case of Li−S−demand a protected Li negative electrode owing to extreme reactivity of metallic Li with H_2O.[273]

5. Conclusions

There have been exciting developments in new positive electrode materials for energy storage in the past decade. Polyanionic compounds have emerged as highly suitable candidates, including $LiFePO_4$ and its olivine analogues such as $LiMnPO_4$, which are starting to make a practical mark. Promising electrochemical properties including excellent cycling stability, low synthetic cost, improved safety characteristics, and low environmental impact are factors that have driven research interest in these compounds. Electrodes comprising nanoparticulate active material exhibit enhanced solid solution behavior and superior electrochemical properties. Many aspects of ion transport, defect chemistry, and solid-solution behavior are not entirely understood, however, and will continue to garner the attention of solid-state electrochemists and theoreticians. Fluorophosphates and silicates, such as $LiVPO_4F$, Na_2FePO_4F, and Li_2FeSiO_4, are also promising new materials. The relatively low ionic and electronic conductivity of these polyanionic compounds brings to the forefront the importance of nanoscale synthesis methods and particle engineering to mitigate these materials' shortcomings.

Layered, spinel, and nanostructured lithium metal oxides still remain among the most viable materials, including $LiCo_{1/3}Ni_{1/3}Mn_{1/3}O_2$ and the composite materials $xLi_2MnO_3\cdot(1-x)LiMO_2$. Very good electrochemical behavior, low synthetic cost, and high gravimetric and volumetric energy densities are factors that have driven research interest in these compounds, and will continue to do so. Nonetheless, safety concerns and the relatively high raw-materials cost of the layered oxides such as $LiCo_{1/3}Ni_{1/3}Mn_{1/3}O_2$ may prohibit their widespread implementation in large-scale energy storage. Aspects of metal ion ordering, the distinction between solid-solution behavior and nanodomain structure, and the nature of the activation process in the composite oxides remain to be uncovered. Future research will involve methods to increase the rate capability of bulk composite materials $xLi_2MnO_3\cdot(1-x)LiMO_2$. Increasingly, clever combinations of lithium metal oxides with lithium metal phosphates to form nanoscaled materials will encompass the advantages of both materials.

Finally, the promise of ultrahigh capacity systems such as Li−S and Li−air offer tantalizing opportunities at present, although they are still very much in their infancy vis a vis intercalation positive electrodes. They will require additional investigation to explore their potential, and will undoubtedly command burgeoning interest.

Acknowledgment. L.F.N. gratefully acknowledges NSERC for financial assistance through the Discovery Grant, Collaborative Grant. and Canada Research Chair programs.

References

(1) Whittingham, M. S. U.S. Patent 4 009 052, **1977**. Haering, R. R.; Stiles, J. A. R.; Brandt, K. U.S. Patent 4 224 390, **1980**. For a review of LiB and Li-ION batteries, see: Whittingham, M.S *Chem. Rev.* **2004**, *104*, 4271.

(2) Mitzushima, K.; Jones, P. C.; Wiseman, P. J.; Goodenough, J. B. *Mater. Res. Bull.* **1980**, *15*, 783. Nagaura, T.; Tozawa, K. *Prog. Batteries Sol. Cells* **1990**, *9*, 209.

(3) Nanjundaswamy, K. S.; Padhi, A. K.; Goodenough, J. B.; Okada, S.; Ohtsuka, H.; Arai, H.; Yamaki, J. *Solid State Ionics* **1996**, *92*, 1–10.

(4) Padhi, A. K.; Nanjundaswamy, K. S.; Masquelier, C.; Okada, S.; Goodenough, J. B. *J. Electrochem. Soc.* **1997**, *144*, 1609–1613.

(5) Padhi, A. K.; Nanjundaswamy, K. S.; Goodenough, J. B. *J. Electrochem. Soc.* **1997**, *144*, 1188–1194.

(6) Koltypin, M.; Aurbach, D.; Nazar, L.; Ellis, B. *Electrochem. Solid-State Lett.* **2007**, *10*, A40–A44.

(7) MacNeil, D. D.; Lu, Z. H.; Chen, Z. H.; Dahn, J. R. *J. Power Sources* **2002**, *108*, 8–14.

(8) Andersson, A. S.; Kalska, B.; Haggstrom, L.; Thomas, J. O. *Solid State Ion.* **2000**, *130*, 41–52.

(9) Huang, H.; Yin, S. C.; Nazar, L. F. *Electrochem. Solid-State Lett.* **2001**, *4*, A170–A172.

(10) Yamada, A.; Chung, S. C.; Hinokuma, K. *J. Electrochem. Soc.* **2001**, *148*, A224–A229.

(11) Prosini, P. P.; Zane, D.; Pasquali, M. *Electrochim. Acta* **2001**, *46*, 3517–3523.

(12) Chen, Z. H.; Dahn, J. R. *J. Electrochem. Soc.* **2002**, *149*, A1184–A1189.

(13) Takahashi, M.; Tobishima, S.; Takei, K.; Sakurai, Y. *Solid State Ionics* **2002**, *148*, 283–289.

(14) Herstedt, M.; Stjerndahl, M.; Nyten, A.; Gustafsson, T.; Rensmo, H.; Siegbahn, H.; Ravet, N.; Armand, M.; Thomas, J. O.; Edstrom, K. *Electrochem. Solid-State Lett.* **2003**, *6*, A202–A206.

(15) Barker, J.; Saidi, M. Y.; Swoyer, J. L. *Electrochem. Solid-State Lett.* **2003**, *6*, A53–A55.

(16) Yonemura, M.; Yamada, A.; Takei, Y.; Sonoyama, N.; Kanno, R. *J. Electrochem. Soc.* **2004**, *151*, A1352–A1356.

(17) Burba, C. M.; Frech, R. *J. Electrochem. Soc.* **2004**, *151*, A1032–A1038.

(18) Kalaiselvi, N.; Doh, C. H.; Park, C. W.; Moon, S. I.; Yun, M. S. *Electrochem. Commun.* **2004**, *6*, 1110–1113.

(19) Franger, S.; Bourbon, C.; Le Cras, F. *J. Electrochem. Soc.* **2004**, *151*, A1024–A1027.

(20) Liao, X. Z.; Ma, Z. F.; Wang, L.; Zhang, X. M.; Jiang, Y.; He, Y. S. *Electrochem. Solid-State Lett.* **2004**, *7*, A522–A525.

(21) Mi, C. H.; Zhao, X. B.; Cao, G. S.; Tu, J. P. *J. Electrochem. Soc.* **2005**, *152*, A483–A487.

(22) Ravet, N.; Besner, S.; Simoneau, M.; Vallee, A.; Armand, M.; Magnan, J.-F. U.S. Patent 6 855 273 B2, **2005**.

(23) Amine, K.; Liu, J.; Belharouak, I. *Electrochem. Commun.* **2005**, *7*, 669–673.

(24) Wang, Y. G.; Wang, Y. R.; Hosono, E. J.; Wang, K. X.; Zhou, H. S. *Angew. Chem., Int. Ed.* **2008**, *47*, 7461–7465.

(25) Prosini, P. P.; Carewska, M.; Scaccia, S.; Wisniewski, P.; Passerini, S.; Pasquali, M. *J. Electrochem. Soc.* **2002**, *149*, A886–A890.

(26) Arnold, G.; Garche, J.; Hemmer, R.; Strobele, S.; Vogler, C.; Wohlfahrt-Mehrens, A. *J. Power Sources* **2003**, *119*−*121*, 247–251.

(27) Hu, Y. Q.; Doeff, M. M.; Kostecki, R.; Finones, R. *J. Electrochem. Soc.* **2004**, *151*, A1279–A1285.

(28) Park, K. S.; Kang, K. T.; Lee, S. B.; Kim, G. Y.; Park, Y. J.; Kim, H. G. *Mater. Res. Bull.* **2004**, *39*, 1803–1810.

(29) Wang, G. X.; Bewlay, S.; Yao, J.; Ahn, J. H.; Dou, S. X.; Liu, H. K. *Electrochem. Solid-State Lett.* **2004**, *7*, A503–A506.

(30) Hsu, K. F.; Tsay, S. Y.; Hwang, B. J. *J. Mater. Chem.* **2004**, *14*, 2690–2695.

(31) Delacourt, C.; Poizot, P.; Tarascon, J. M.; Masquelier, C. *Nat. Mater.* **2005**, *4*, 254–260.

(32) Delacourt, C.; Poizot, P.; Levasseur, S.; Masquelier, C. *Electrochem. Solid-State Lett.* **2006**, *9*, A352–A355.

(33) Kim, D. H.; Kim, J. *Electrochem. Solid-State Lett.* **2006**, *9*, A439–A442.

(34) Kim, D. H.; Kim, J. S.; Kang, J. W.; Kim, E. J.; Ahn, H. Y.; Kim, J. *J. Nanosci. Nanotechnol.* **2007**, *8*, 3949–3953.

(35) Recham, N.; Dupont, L.; Courty, M.; Djellab, K.; Larcher, D.; Armand, M.; Tarascon, J. M. *Chem. Mater.* **2009**, *21*, 1096–1107.

(36) Yang, S. F.; Zavalij, P. Y.; Whittingham, M. S. *Electrochem. Commun.* **2001**, *3*, 505–508.

(37) Chen, J. J.; Whittingham, M. S. *Electrochem. Commun.* **2006**, *8*, 855–858.

(38) Ellis, B.; Kan, W. H.; Makahnouk, W. R. M.; Nazar, L. F. *J. Mater. Chem.* **2007**, *17*, 3248–3254.

(39) Franger, S.; Le Cras, F.; Bourbon, C.; Rouault, H. *J. Power Sources* **2003**, *119*−*121*, 252–257.

(40) Dokko, K.; Koizumi, S.; Kanamura, K. *Chem. Lett.* **2006**, *35*, 338–339.

(41) Murugan, A. V.; Muraliganth, T.; Manthiram, A. *Electrochem. Commun.* **2008**, *10*, 903–906.

(42) Yoon, W. S.; Paik, Y.; Yang, X. Q.; Balasubramanian, M.; McBreen, J.; Grey, C. P. *Electrochem. Solid-State Lett.* **2002**, *5*, A263–A266.

(43) Fang, H. S.; Pan, Z. Y.; Li, L. P.; Yang, Y.; Yan, G. F.; Li, G. S.; Wei, S. Q. *Electrochem. Commun.* **2008**, *10*, 1071–1073.

(44) Morgan, D.; Van der Ven, A.; Ceder, G. *Electrochem. Solid-State Lett.* **2004**, *7*, A30–A32.

(45) Islam, M. S.; Driscoll, D. J.; Fisher, C. A. J.; Slater, P. R. *Chem. Mater.* **2005**, *17*, 5085–5092.

(46) Nishimura, S.; Kobayashi, G.; Ohoyama, K.; Kanno, R.; Yashima, M.; Yamada, A. *Nat. Mater.* **2008**, *7*, 707–711.

(47) Li, J. Y.; Yao, W. L.; Martin, S.; Vaknin, D. *Solid State Ionics* **2008**, *179*, 2016–2019.

(48) Amin, R.; Maier, J.; Balaya, P.; Chen, D. P.; Lin, C. T. *Solid State Ionics* **2008**, *179*, 1683–1687.

(49) Maxisch, T.; Zhou, F.; Ceder, G. *Phys. Rev. B* **2006**, 73.

(50) (a) Ellis, B.; Perry, L. K.; Ryan, D. H.; Nazar, L. F. *J. Am. Chem. Soc.* **2006**, *128*, 11416–11422. (b) Lee, K. T.; Kan, W. H.; Nazar, L. F. *J. Am. Chem. Soc.* **2009**, *131*, 6044–6045.

(51) Chung, S. Y.; Bloking, J. T.; Chiang, Y. M. *Nat. Mater.* **2002**, *1*, 123–128.

(52) Srinivasan, V.; Newman, J. *J. Electrochem. Soc.* **2004**, *151*, A1517–A1529.

(53) Wang, L.; Zhou, F.; Meng, Y. S.; Ceder, G. *Phys. Rev. B* **2007**, 76.

(54) Fisher, C. A. J.; Islam, M. S. *J. Mater. Chem.* **2008**, *18*, 1209–1215.

(55) Chen, G. Y.; Song, X. Y.; Richardson, T. J. *Electrochem. Solid-State Lett.* **2006**, *9*, A295–A298.

(56) Laffont, L.; Delacourt, C.; Gibot, P.; Wu, M. Y.; Kooyman, P.; Masquelier, C.; Tarascon, J. M. *Chem. Mater.* **2006**, *18*, 5520–5529.

(57) Delmas, C.; Maccario, M.; Croguennec, L.; Le Cras, F.; Weill, F. *Nat. Mater.* **2008**, *7*, 665–671.

(58) Yamada, A.; Kudo, Y.; Liu, K. Y. *J. Electrochem. Soc.* **2001**, *148*, A747–A754.

(59) Yamada, A.; Koizumi, H.; Sonoyama, N.; Kanno, R. *Electrochem. Solid-State Lett.* **2005**, *8*, A409–A413.

(60) Yamada, A.; Koizumi, H.; Nishimura, S. I.; Sonoyama, N.; Kanno, R.; Yonemura, M.; Nakamura, T.; Kobayashi, Y. *Nat. Mater.* **2006**, *5*, 357–360.

(61) Meethong, N.; Huang, H. Y. S.; Carter, W. C.; Chiang, Y. M. *Electrochem. Solid-State Lett.* **2007**, *10*, A134–A138.

(62) Wagemaker, M.; Borghols, W. J. H.; Mulder, F. M. *J. Am. Chem. Soc.* **2007**, *129*, 4323–4327.

(63) Kobayashi, G.; Nishimura, S. I.; Park, M. S.; Kanno, R.; Yashima, M.; Ida, T.; Yamada, A. *Adv. Funct. Mater.* **2009**, *19*, 395–403.

(64) Delacourt, C.; Rodriguez-Carvajal, J.; Schmitt, B.; Tarascon, J. M.; Masquelier, C. *Solid State Sci.* **2005**, *7*, 1506–1516.

(65) Dodd, J. L.; Halevy, I.; Fultz, B. *J. Phys. Chem. C* **2007**, *111*, 1563–1566.

(66) Dodd, J. L.; Yazami, R.; Fultz, B. *Electrochem. Solid-State Lett.* **2006**, *9*, A151–A155.

(67) Gibot, P.; Casas-Cabanas, M.; Laffont, L.; Levasseur, S.; Carlach, P.; Hamelet, S.; Tarascon, J. M.; Masquelier, C. *Nat. Mater.* **2008**, *7*, 741–747.

(68) Ravet, N.; Abouimrane, A.; Armand, M. *Nat. Mater.* **2003**, *2*, 702–702.

(69) Herle, P. S.; Ellis, B.; Coombs, N.; Nazar, L. F. *Nat. Mater.* **2004**, *3*, 147–152.

(70) Ellis, B.; Herle, P. S.; Rho, Y. H.; Nazar, L. F.; Dunlap, R.; Perry, L. K.; Ryan, D. H. *Faraday Discuss.* **2007**, *134*, 119–141.

(71) Delacourt, C.; Wurm, C.; Laffont, L.; Leriche, J. B.; Masquelier, C. *Solid State Ionics* **2006**, *177*, 333–341.

(72) Fisher, C. A. J.; Prieto, V. M. H.; Islam, M. S. *Chem. Mater.* **2008**, *20*, 5907–5915.

(73) Goni, A.; Lezama, L.; Pujana, A.; Arriortua, M. I.; Rojo, T. *Int. J. Inorg. Mater.* **2001**, *3*, 937–942.

(74) Goni, A.; Lezama, L.; Arriortua, M. I.; Barberis, G. E.; Rojo, T. *J. Mater. Chem.* **2000**, *10*, 423–428.

(75) Wagemaker, M.; Ellis, B. L.; Luetzenkirchen-Hecht, D.; Mulder, F. M.; Nazar, L. F. *Chem. Mater.* **2008**, *20*, 6313–6315.

(76) Meethong, N.; Kao, Y. H.; Speakman, S. A.; Chiang, Y. M. *Adv. Funct. Mater.* **2009**, *19*, 1060–1070.

(77) Rho, Y. H.; Nazar, L. F.; Perry, L.; Ryan, D. *J. Electrochem. Soc.* **2007**, *154*, A283–A289.

(78) Kang, B.; Ceder, G. *Nature* **2009**, *458*, 190–193.

(79) Zaghib, K.; Goodenough, J. B.; Mauger, A.; Julien, C. J. Power Sources **2009**, in press.

(80) Doeff, M. M.; Wilcox, J. D.; Kostecki, R.; Lau, G. *J. Power Sources* **2006**, *163*, 180–184.

(81) Dominko, R.; Bele, M.; Gaberscek, M.; Remskar, M.; Hanzel, D.; Pejovnik, S.; Jamnik, J. *J. Electrochem. Soc.* **2005**, *152*, A607–A610.

(82) Delacourt, C.; Poizot, P.; Morcrette, M.; Tarascon, J. M.; Masquelier, C. *Chem. Mater.* **2004**, *16*, 93–99.

(83) Dominko, R.; Bele, M.; Gaberscek, M.; Remskar, M.; Hanzel, D.; Goupil, J. M.; Pejovnik, S.; Jamnik, J. *J. Power Sources* **2006**, *153*, 274–280.

(84) Yang, J. S.; Xu, J. J. *J. Electrochem. Soc.* **2006**, *153*, A716–A723.
(85) Drezen, T.; Kwon, N. H.; Bowen, P.; Teerlinck, I.; Isono, M.; Exnar, I. *J. Power Sources* **2007**, *174*, 949–953.
(86) Wang, D. Y.; Buqa, H.; Crouzet, M.; Deghenghi, G.; Drezen, T.; Exnar, I.; Kwon, N. H.; Miners, J. H.; Poletto, L.; Graetzel, M. *J. Power Sources* **2009**, *189*, 624–628.
(87) Shiratsuchi, T.; Okada, S.; Doi, T.; Yamaki, J. *Electrochim. Acta* **2009**, *54*, 3145–3151.
(88) Chen, G. Y.; Wilcox, J. D.; Richardson, T. J. *Electrochem. Solid-State Lett.* **2008**, *11*, A190–A194.
(89) Guoying, C.; Thomas, J. R. *J. Electrochem. Soc.* **2009**, *156*, A756–A762.
(90) Kim, S.-W.; Kim, J.; Gwon, H.; Kang, K. *J. Electrochem. Soc.* **2009**, *156*, A635–A638.
(91) Barker, J.; Saidi, M. Y.; Swoyer, J. L. *J. Electrochem. Soc.* **2003**, *150*, A1394–A1398.
(92) Pizarro-Sanz, J. L.; Dance, J. M.; Villeneuve, G.; Arriortua-Marcaida, M. I. *Mater. Lett.* **1994**, *18*, 327–330.
(93) Groat, L. A.; Raudsepp, M.; Hawthorne, F. C.; Ercit, T. S.; Sherriff, B. L.; Hartman, J. S. *Am. Mineral.* **1990**, *75*, 992–1008.
(94) Barker, J.; Gover, R. K. B.; Burns, P.; Bryan, A.; Saidi, M. Y.; Swoyer, J. L. *J. Power Sources* **2005**, *146*, 516–520.
(95) Makimura, Y.; Cahill, L. S.; Iriyama, Y.; Goward, G. R.; Nazar, L. F. *Chem. Mater.* **2008**, *20*, 4240–4248.
(96) Barker, J.; Gover, R. K. B.; Burns, P.; Bryan, A. J. *Electrochem. Solid-State Lett.* **2006**, *9*, A190–A192.
(97) (a) Ellis, B. L.; Makahnouk, W. R. M.; Makimura, Y.; Toghill, K.; Nazar, L. F. *Nat. Mater.* **2007**, *6*, 749−753. (b) Ellis, B. L.; Makahnouk, W. R. M.; Rowan-Weetaluktuk, W. N.; Ryan, D. H.; Nazar, L. F. *Chem. Mater.* **2009**, DOI: 10.1021/cm902023h.
(98) Sanz, F.; Parada, C.; Ruiz-Valero, C. *J. Mater. Chem.* **2001**, *11*, 208–211.
(99) Swafford, S. H.; Holt, E. M. *Solid State Sci.* **2002**, *4*, 807–812.
(100) Yakubovich, O. V.; Karimova, O. V.; Melnikov, O. K. *Acta Crystallogr., Sect. C* **1997**, *53*, 395–397.
(101) Dutreilh, M.; Chevalier, C.; El-Ghozzi, M.; Avignant, D.; Montel, J. M. *J. Solid State Chem.* **1999**, *142*, 1–5.
(102) Okada, S.; Ueno, M.; Uebou, Y.; Yamaki, J. *J. Power Sources* **2005**, *146*, 565–569.
(103) Keffer, C.; Mighell, A.; Mauer, F.; Swanson, H.; Block, S. *Inorg. Chem.* **1967**, *6*, 119–125.
(104) Zemann, J. *Acta Crystallogr.* **1960**, *13*, 863–867.
(105) Nyten, A.; Abouimrane, A.; Armand, M.; Gustafsson, T.; Thomas, J. O. *Electrochem. Commun.* **2005**, *7*, 156–160.
(106) Nyten, A.; Kamali, S.; Haggstrom, L.; Gustafsson, T.; Thomas, J. O. *J. Mater. Chem.* **2006**, *16*, 2266–2272.
(107) Zaghib, K.; Salah, A. A.; Ravet, N.; Mauger, A.; Gendron, F.; Julien, C. M. *J. Power Sources* **2006**, *160*, 1381–1386.
(108) Kokalj, A.; Dominko, R.; Mali, G.; Meden, A.; Gaberscek, M.; Jamnik, J. *Chem. Mater.* **2007**, *19*, 3633–3640.
(109) Dominko, R.; Bele, M.; Gaberscek, M.; Meden, A.; Remskar, M.; Jamnik, J. *Electrochem. Commun.* **2006**, *8*, 217–222.
(110) Dominko, R. *J. Power Sources* **2008**, *184*, 462–468.
(111) Arroyo-DeDompablo, M. E.; Dominko, R.; Gallardo-Amores, J. M.; Dupont, L.; Mali, G.; Ehrenberg, H.; Jamnik, J.; Moran, E. *Chem. Mater.* **2008**, *20*, 5574–5584.
(112) West, A. R.; Glasser, F. P. *J. Solid State Chem.* **1972**, *4*, 20–&.
(113) Lyness, C.; Delobel, B.; Armstrong, A. R.; Bruce, P. G. *Chem. Commun.* **2007**, 4890–4892.
(114) Wolfenstine, J.; Allen, J. *J. Power Sources* **2004**, *136*, 150–153.
(115) Amine, K.; Yasuda, H.; Yamachi, M. *Electrochem. Solid-State Lett.* **2000**, *3*, 178–179.
(116) Arroyo-, M. E.; Armand, M.; Tarascon, J. M.; Amador, U. *Electrochem. Commun.* **2006**, *8*, 1292–1298.
(117) Mizushima, K.; Jones, P. C.; Wiseman, P. J.; Goodenough, J. B. *Mater. Res. Bull.* **1980**, *15*, 783–789.
(118) Ohzuku, T.; Ueda, A. *J. Electrochem. Soc.* **1994**, *141*, 2972–2977.
(119) Yang, X. Q.; Sun, X.; McBreen, J. *Electrochem. Commun.* **2000**, *2*, 100–103.
(120) Reimers, J. N.; Dahn, J. R. *J. Electrochem. Soc.* **1992**, *139*, 2091–2097.
(121) Amatucci, G. G.; Tarascon, J. M.; Klein, L. C. *J. Electrochem. Soc.* **1996**, *143*, 1114–1123.
(122) Van der Ven, A.; Aydinol, M. K.; Ceder, G. *J. Electrochem. Soc.* **1998**, *145*, 2149–2155.
(123) Chen, Z. H.; Lu, Z. H.; Dahn, J. R. *J. Electrochem. Soc.* **2002**, *149*, A1604–A1609.
(124) Wang, H. F.; Jang, Y. I.; Huang, B. Y.; Sadoway, D. R.; Chiang, Y. T. *J. Electrochem. Soc.* **1999**, *146*, 473–480.
(125) Endo, E.; Yasuda, T.; Kita, A.; Yamaura, K.; Sekai, K. *J. Electrochem. Soc.* **2000**, *147*, 1291–1294.
(126) Chung, K. Y.; Yoon, W. S.; McBreen, J.; Yang, X. Q.; Oh, S. H.; Shin, H. C.; Il Cho, W.; Cho, B. W. *J. Electrochem. Soc.* **2006**, *153*, A2152–A2157.
(127) Amatucci, G. G.; Tarascon, J. M.; Klein, L. C. *Solid State Ionics* **1996**, *83*, 167–173.
(128) Luo, W. B.; Dahn, J. R. *Electrochim. Acta* **2009**, *54*, 4655–4661.
(129) Jang, Y. I.; Huang, B. Y.; Wang, H. F.; Sadoway, D. R.; Ceder, G.; Chiang, Y. M.; Liu, H.; Tamura, H. *J. Electrochem. Soc.* **1999**, *146*, 862–868.
(130) Jones, C. D. W.; Rossen, E.; Dahn, J. R. *Solid State Ionics* **1994**, *68*, 65–69.
(131) Cho, J.; Kim, Y. J.; Kim, T. J.; Park, B. *Angew. Chem., Int. Ed.* **2001**, *40*, 3367–+.
(132) Cho, J.; Kim, Y. W.; Kim, B.; Lee, J. G.; Park, B. *Angew. Chem., Int. Ed.* **2003**, *42*, 1618–1621.
(133) Chen, Z. H.; Dahn, J. R. *Electrochem. Solid-State Lett.* **2004**, *7*, A11–A14.
(134) Chen, Z. H.; Dahn, J. R. *Electrochim. Acta* **2004**, *49*, 1079–1090.
(135) Amatucci, G.; Tarascon, J. M. *J. Electrochem. Soc.* **2002**, *149*, K31–K46.
(136) Tarascon, J. M.; Guyomard, D.; Baker, G. L. *J. Power Sources* **1993**, *44*, 689–700.
(137) Tarascon, J. M.; Guyomard, D. *Electrochim. Acta* **1993**, *38*, 1221–1231.
(138) Thackeray, M. M.; Shao-Horn, Y.; Kahaian, A. J.; Kepler, K. D.; Vaughey, J. T.; Hackney, S. A. *Electrochem. Solid-State Lett.* **1998**, *1*, 7–9.
(139) Jang, D. H.; Shin, Y. J.; Oh, S. M. *J. Electrochem. Soc.* **1996**, *143*, 2204–2211.
(140) Huang, H.; Vincent, C. A.; Bruce, P. G. *J. Electrochem. Soc.* **1999**, *146*, 3649–3654.
(141) Shin, Y. J.; Manthiram, A. *J. Electrochem. Soc.* **2004**, *151*, A204–A208.
(142) Deng, B. H.; Nakamura, H.; Yoshio, M. *J. Power Sources* **2008**, *180*, 864–868.
(143) Aurbach, D.; Talyosef, Y.; Markovsky, B.; Markevich, E.; Zinigrad, E.; Asraf, L.; Gnanaraj, J. S.; Kim, H. J. *Electrochim. Acta* **2004**, *50*, 247–254.
(144) Hunter, J. C. *J. Solid State Chem.* **1981**, *39*, 142–147.
(145) Benedek, R.; Thackeray, M. M. *Electrochem. Solid-State Lett.* **2006**, *9*, A265–A267.
(146) Lee, Y. S.; Yoshio, M. *Electrochem. Solid-State Lett.* **2001**, *4*, A155–A158.
(147) Xia, Y. G.; Zhang, Q.; Wang, H. Y.; Nakamura, H.; Noguchi, H.; Yoshio, M. *Electrochim. Acta* **2007**, *52*, 4708–4714.
(148) Manthiram, A.; Choi, W. *Electrochem. Solid-State Lett.* **2007**, *10*, A228–A231.
(149) Jiao, F.; Bao, J. L.; Hill, A. H.; Bruce, P. G. *Angew. Chem., Int. Ed.* **2008**, *47*, 9711–9716.
(150) Kim, D. K.; Muralidharan, P.; Lee, H. W.; Ruffo, R.; Yang, Y.; Chan, C. K.; Peng, H.; Huggins, R. A.; Cui, Y. *Nano Lett.* **2008**, *8*, 3948–3952.
(151) Wakihara, M. *Electrochemistry* **2005**, *73*, 328–335.
(152) Kunduraci, M.; Amatucci, G. G. *Electrochim. Acta* **2008**, *53*, 4193–4199.
(153) Talyosef, Y.; Markovsky, B.; Salitra, G.; Aurbach, D.; Kim, H. J.; Choi, S. *J. Power Sources* **2005**, *146*, 664–669.
(154) Park, S. H.; Oh, S. W.; Kang, S. H.; Belharouak, I.; Amine, K.; Sun, Y. K. *Electrochim. Acta* **2007**, *52*, 7226–7230.
(155) Shaju, K. M.; Bruce, P. G. *Dalton Trans.* **2008**, 5471–5475.
(156) Imazaki, M.; Ariyoshi, K.; Ohzuku, T. *J. Electrochem. Soc.* **2009**, *156*, A780–A786.
(157) Dahn, J. R.; Vonsacken, U.; Michal, C. A. *Solid State Ionics* **1990**, *44*, 87–97.
(158) Rougier, A.; Gravereau, P.; Delmas, C. *J. Electrochem. Soc.* **1996**, *143*, 1168–1175.
(159) Pouillerie, C.; Suard, E.; Delmas, C. *J. Solid State Chem.* **2001**, *158*, 187–197.
(160) Pouillerie, C.; Croguennec, L.; Biensan, P.; Willmann, P.; Delmas, C. *J. Electrochem. Soc.* **2000**, *147*, 2061–2069.
(161) Saadoune, I.; Delmas, C. *J. Mater. Chem.* **1996**, *6*, 193–199.
(162) Rougier, A.; Saadoune, I.; Gravereau, P.; Willmann, P.; Delmas, C. *Solid State Ionics* **1996**, *90*, 83–90.
(163) Zhecheva, E.; Stoyanova, R. *Solid State Ionics* **1993**, *66*, 143–149.
(164) Chebiam, R. V.; Prado, F.; Manthiram, A. *J. Electrochem. Soc.* **2001**, *148*, A49–A53.
(165) Naghash, A. R.; Lee, J. Y. *Electrochim. Acta* **2001**, *46*, 2293–2304.
(166) Park, S. H.; Sun, Y. K.; Park, K. S.; Nahm, K. S.; Lee, Y. S.; Yoshio, M. *Electrochim. Acta* **2002**, *47*, 1721–1726.
(167) Ohzuku, T.; Ueda, A.; Nagayama, M. *J. Electrochem. Soc.* **1993**, *140*, 1862–1870.
(168) Li, W.; Reimers, J. N.; Dahn, J. R. *Solid State Ionics* **1993**, *67*, 123–130.
(169) Mishra, S. K.; Ceder, G. *Phys. Rev. B* **1999**, *59*, 6120–6130.
(170) Armstrong, A. R.; Bruce, P. G. *Nature* **1996**, *381*, 499–500.
(171) Capitaine, F.; Gravereau, P.; Delmas, C. *Solid State Ionics* **1996**, *89*, 197–202.
(172) Vitins, G.; West, K. *J. Electrochem. Soc.* **1997**, *144*, 2587–2592.
(173) Ceder, G.; Van der Ven, A. *Electrochim. Acta* **1999**, *45*, 131–150.
(174) Robertson, A. D.; Armstrong, A. R.; Bruce, P. G. *Chem. Mater.* **2001**, *13*, 2380–2386.
(175) Paulsen, J. M.; Thomas, C. L.; Dahn, J. R. *J. Electrochem. Soc.* **1999**, *146*, 3560–3565.
(176) Paulsen, J. M.; Thomas, C. L.; Dahn, J. R. *J. Electrochem. Soc.* **2000**, *147*, 861–868.
(177) Rossen, E.; Jones, C. D. W.; Dahn, J. R. *Solid State Ionics* **1992**, *57*, 311–318.
(178) Ohzuku, T.; Makimura, Y. *Chem. Lett.* **2001**, 744–745.

(179) Lu, Z. H.; MacNeil, D. D.; Dahn, J. R. *Electrochem. Solid-State Lett.* **2001**, *4*, A191–A194.
(180) Ohzuku, T.; Makimura, Y. *Chem. Lett.* **2001**, 642–643.
(181) Makimura, Y.; Ohzuku, T. *J. Power Sources* **2003**, *119*, 156–160.
(182) Zhou, F.; Zhao, X. M.; Lu, Z. H.; Jiang, J. W.; Dahn, J. R. *Electrochem. Solid-State Lett.* **2008**, *11*, A155–A157.
(183) Yabuuchi, N.; Kim, Y. T.; Li, H. H.; Shao-Horn, Y. *Chem. Mater.* **2008**, *20*, 4936–4951.
(184) Spahr, M. E.; Novak, P.; Schnyder, B.; Haas, O.; Nesper, R. *J. Electrochem. Soc.* **1998**, *145*, 1113–1121.
(185) Ammundsen, B.; Paulsen, J. *Adv. Mater.* **2001**, *13*, 943–+.
(186) Reed, J.; Ceder, G. *Electrochem. Solid-State Lett.* **2002**, *5*, A145–A148.
(187) Miao, S.; Kocher, M.; Rez, P.; Fultz, B.; Ozawa, Y.; Yazami, R.; Ahn, C. C. *J. Phys. Chem. B* **2005**, *109*, 23473–23479.
(188) Islam, M. S.; Davies, R. A.; Gale, J. D. *Chem. Mater.* **2003**, *15*, 4280–4286.
(189) Venkatraman, S.; Choi, J.; Manthiram, A. *Electrochem. Commun.* **2004**, *6*, 832–837.
(190) Kang, K.; Ceder, G. *Phys. Rev. B* **2006**, *74*, 09415.
(191) Kang, K. S.; Meng, Y. S.; Breger, J.; Grey, C. P.; Ceder, G. *Science* **2006**, *311*, 977–980.
(192) Schougaard, S. B.; Breger, J.; Jiang, M.; Grey, C. P.; Goodenough, J. B. *Adv. Mater.* **2006**, *18*, 905–+.
(193) Wu, E. J.; Tepesch, P. D.; Ceder, G. *Philos. Mag., B* **1998**, *77*, 1039–1047.
(194) Breger, J.; Meng, Y. S.; Hinuma, Y.; Kumar, S.; Kang, K.; Shao-Horn, Y.; Ceder, G.; Grey, C. P. *Chem. Mater.* **2006**, *18*, 4768–4781.
(195) Grey, C. P.; Yoon, W. S.; Reed, J.; Ceder, G. *Electrochem. Solid-State Lett.* **2004**, *7*, A290–A293.
(196) Yabuuchi, N.; Kumar, S.; Li, H. H.; Kim, Y. T.; Shao-Horn, Y. *J. Electrochem. Soc.* **2007**, *154*, A566–A578.
(197) Lu, Z. H.; Chen, Z. H.; Dahn, J. R. *Chem. Mater.* **2003**, *15*, 3214–3220.
(198) Yoon, W. S.; Iannopollo, S.; Grey, C. P.; Carlier, D.; Gorman, J.; Reed, J.; Ceder, G. *Electrochem. Solid-State Lett.* **2004**, *7*, A167–A171.
(199) Meng, Y. S.; Ceder, G.; Grey, C. P.; Yoon, W. S.; Shao-Horn, Y. *Electrochem. Solid-State Lett.* **2004**, *7*, A155–A158.
(200) Chemova, N. A.; Ma, M.; Xiao, J.; Whittingham, M. S.; Breger, J.; Grey, C. P. *Chem. Mater.* **2007**, *19*, 4682–4693.
(201) Van der Ven, A.; Ceder, G. *Electrochem. Commun.* **2004**, *6*, 1045–1050.
(202) Koyama, Y.; Makimura, Y.; Tanaka, I.; Adachi, H.; Ohzuku, T. *J. Electrochem. Soc.* **2004**, *151*, A1499–A1506.
(203) Breger, J.; Kang, K.; Cabana, J.; Ceder, G.; Grey, C. P. *J. Mater. Chem.* **2007**, *17*, 3167–3174.
(204) Breger, J.; Dupre, N.; Chupas, P. J.; Lee, P. L.; Proffen, T.; Parise, J. B.; Grey, C. P. *J. Am. Chem. Soc.* **2005**, *127*, 7529–7537.
(205) Hinuma, Y.; Meng, Y. S.; Kang, K. S.; Ceder, G. *Chem. Mater.* **2007**, *19*, 1790–1800.
(206) Yang, X. Q.; McBreen, J.; Yoon, W. S.; Grey, C. P. *Electrochem. Commun.* **2002**, *4*, 649–654.
(207) Venkatraman, S.; Manthiram, A. *Chem. Mater.* **2003**, *15*, 5003–5009.
(208) Arachi, Y.; Kobayashi, H.; Emura, S.; Nakata, Y.; Tanaka, M.; Asai, T. *Chem. Lett.* **2003**, *32*, 60–61.
(209) Arachi, Y.; Kobayashi, H.; Emura, S.; Nakata, Y.; Tanaka, M.; Asai, T.; Sakaebe, H.; Tatsumi, K.; Kageyama, H. *Solid State Ionics* **2005**, *176*, 895–903.
(210) Koyama, Y.; Tanaka, I.; Adachi, H.; Makimura, Y.; Ohzuku, T. *J. Power Sources* **2003**, *119*, 644–648.
(211) Hwang, B. J.; Tsai, Y. W.; Carlier, D.; Ceder, G. *Chem. Mater.* **2003**, *15*, 3676–3682.
(212) Lu, Z. H.; MacNeil, D. D.; Dahn, J. R. *Electrochem. Solid-State Lett.* **2001**, *4*, A200–A203.
(213) Yin, S. C.; Rho, Y. H.; Swainson, I.; Nazar, L. F. *Chem. Mater.* **2006**, *18*, 1901–1910.
(214) Kobayashi, H.; Arachi, Y.; Emura, S.; Kageyama, H.; Tatsumi, K.; Kamiyama, T. *J. Power Sources* **2005**, *146*, 640–644.
(215) Whitfield, P. S.; Davidson, I. J.; Cranswick, L. M. D.; Swainson, I. P.; Stephens, P. W. *Solid State Ionics* **2005**, *176*, 463–471.
(216) Kim, J. M.; Chung, H. T. *Electrochim. Acta* **2004**, *49*, 937–944.
(217) Reale, P.; Privitera, D.; Panero, S.; Scrosati, B. *Solid State Ionics* **2007**, *178*, 1390–1397.
(218) Cahill, L. S.; Yin, S. C.; Samoson, A.; Heinmaa, I.; Nazar, L. F.; Goward, G. R. *Chem. Mater.* **2005**, *17*, 6560–6566.
(219) Yoshio, M.; Noguchi, H.; Itoh, J.; Okada, M.; Mouri, T. *J. Power Sources* **2000**, *90*, 176–181.
(220) Yabuuchi, N.; Makimura, Y.; Ohzuku, T. *J. Electrochem. Soc.* **2007**, *154*, A314–A321.
(221) Choi, J.; Manthiram, A. *J. Electrochem. Soc.* **2005**, *152*, A1714–A1718.
(222) Yabuuchi, N.; Ohzuku, T. *J. Power Sources* **2003**, *119*, 171–174.
(223) Wang, Y. D.; Jiang, J. W.; Dahn, J. R. *Electrochem. Commun.* **2007**, *9*, 2534–2540.
(224) Yoon, W. S.; Grey, C. P.; Balasubramanian, M.; Yang, X. Q.; Fischer, D. A.; McBreen, J. *Electrochem. Solid-State Lett.* **2004**, *7*, A53–A55.
(225) Yoon, W. S.; Balasubramanian, M.; Chung, K. Y.; Yang, X. Q.; McBreen, J.; Grey, C. P.; Fischer, D. A. *J. Am. Chem. Soc.* **2005**, *127*, 17479–17487.
(226) Tsai, Y. W.; Hwang, B. J.; Ceder, G.; Sheu, H. S.; Liu, D. G.; Lee, J. F. *Chem. Mater.* **2005**, *17*, 3191–3199.
(227) Yabuuchi, N.; Koyama, Y.; Nakayama, N.; Ohzuku, T. *J. Electrochem. Soc.* **2005**, *152*, A1434–A1440.
(228) Zeng, D. L.; Cabana, J.; Breger, J. L.; Yoon, W. S.; Grey, C. P. *Chem. Mater.* **2007**, *19*, 6277–6289.
(229) Shinova, E.; Stoyanova, R.; Zhecheva, E.; Ortiz, G. F.; Lavela, P.; Tirado, J. L. *Solid State Ionics* **2008**, *179*, 2198–2208.
(230) Thackeray, M. M.; Johnson, C. S.; Vaughey, J. T.; Li, N.; Hackney, S. A. *J. Mater. Chem.* **2005**, *15*, 2257–2267.
(231) Johnson, C. S.; Li, N.; Vaughey, J. T.; Hackney, S. A.; Thackeray, M. M. *Electrochem. Commun.* **2005**, *7*, 528–536.
(232) Kim, J. S.; Johnson, C. S.; Vaughey, J. T.; Thackeray, M. M.; Hackney, S. A. *Chem. Mater.* **2004**, *16*, 1996–2006.
(233) Johnson, C. S.; Li, N. C.; Lefief, C.; Vaughey, J. T.; Thackeray, M. M. *Chem. Mater.* **2008**, *20*, 6095–6106.
(234) Kim, J. S.; Johnson, C. S.; Thackeray, M. M. *Electrochem. Commun.* **2002**, *4*, 205–209.
(235) Rossouw, M. H.; Thackeray, M. M. *Mater. Res. Bull.* **1991**, *26*, 463–473.
(236) Rossouw, M. H.; Liles, D. C.; Thackeray, M. M. *J. Solid State Chem.* **1993**, *104*, 464–466.
(237) Kalyani, P.; Chitra, S.; Mohan, T.; Gopukumar, S. *J. Power Sources* **1999**, *80*, 103.
(238) Yoon, W. S.; Kim, N.; Yang, X. Q.; McBreen, J.; Grey, C. P. J. Power Sources **2003**; Vol. *119*, pp 649−653.
(239) Johnson, C. S.; Kim, J. S.; Lefief, C.; Li, N.; Vaughey, J. T.; Thackeray, M. M. *Electrochem. Commun.* **2004**, *6*, 1085–1091.
(240) Armstrong, A. R.; Holzapfel, M.; Novak, P.; Johnson, C. S.; Kang, S. H.; Thackeray, M. M.; Bruce, P. G. *J. Am. Chem. Soc.* **2006**, *128*, 8694–8698.
(241) Jiang, M.; Key, B.; Meng, Y. S.; Grey, C. P. *Chem. Mater.* **2009**, *21*, 2733–2745.
(242) Johnson, C. S.; Li, N. C.; Lefief, C.; Thackeray, M. M. *Electrochem. Commun.* **2007**, *9*, 787–795.
(243) Kang, S. H.; Thackeray, M. M. *Electrochem. Commun.* **2009**, *11*, 748–751.
(244) Rauh, R. D.; Abraham, K. M.; Pearson, G. F.; Surprenant, J. K.; Brummer, S. B. *J. Electrochem. Soc.* **1979**, *126*, 523–527.
(245) Yamin, H.; Peled, E. *J. Power Sources* **1983**, *9*, 281–287.
(246) Chu, M.-Y. U.S. Patent 5 686 201, **1997**.
(247) Peramunage, D.; Licht, S. *Science* **1993**, *261*, 1029–1032.
(248) Rao, M. L. U.S. Patent 3 413 154, **1968**.
(249) Nole, D.; Moss, V. U.S. Patent 3 532 543, **1970**.
(250) Wang, J. L.; Yang, J.; Xie, J. Y.; Xu, N. X. *Adv. Mater.* **2002**, *14*, 963–+.
(251) Zheng, W.; Liu, Y. W.; Hu, X. G.; Zhang, C. F. *Electrochim. Acta* **2006**, *51*, 1330–1335.
(252) Rauh, R. D.; Shuker, F. S.; Marston, J. M.; Brummer, S. B. *J. Inorg. Nucl. Chem.* **1977**, *39*, 1761–1766.
(253) Cheon, S. E.; Ko, K. S.; Cho, J. H.; Kim, S. W.; Chin, E. Y.; Kim, H. T. *J. Electrochem. Soc.* **2003**, *150*, A800–A805.
(254) Mikhaylik, Y. V.; Akridge, J. R. *J. Electrochem. Soc.* **2004**, *151*, A1969–A1976.
(255) Mikhaylik, Y. V. U.S. Patent 7 354 680, **2008**.
(256) Visco, S. J.; Nimon, Y. S.; Katz, B. D. U.S. Patent 7 282 302, **2007**.
(257) Visco, S. J.; Chu, M. Y. U.S. Patent 6 210 832, **2001**.
(258) Song, M. S.; Han, S. C.; Kim, H. S.; Kim, J. H.; Kim, K. T.; Kang, Y. M.; Ahn, H. J.; Dou, S. X.; Lee, J. Y. *J. Electrochem. Soc.* **2004**, *151*, A791–A795.
(259) Gorkovenko, A.; Skotheim, T. A.; Xu, Z.-S. U.S. Patent 6 878 488 B2, **2005**.
(260) Jeon, B. H.; Yeon, J. H.; Kim, K. M.; Chung, I. J. *J. Power Sources* **2002**, *109*, 89–97.
(261) Marmorstein, D.; Yu, T. H.; Striebel, K. A.; McLarnon, F. R.; Hou, J.; Cairns, E. J. *J. Power Sources* **2000**, *89*, 219–226.
(262) Shim, J.; Striebel, K. A.; Cairns, E. J. *J. Electrochem. Soc.* **2002**, *149*, A1321–A1325.
(263) Shin, J. H.; Cairns, E. J. *J. Power Sources* **2008**, *177*, 537–545.
(264) Shin, J. H.; Cairns, E. J. *J. Electrochem. Soc.* **2008**, *155*, A368–A373.
(265) Ji, X. L.; Lee, K. T.; Nazar, L. F. *Nat. Mater.* **2009**, *8*, 500–506.
(266) Abraham, K. M.; Jiang, Z. *J. Electrochem. Soc.* **1996**, *143*, 1–5.
(267) Ogasawara, T.; Debart, A.; Holzapfel, M.; Novak, P.; Bruce, P. G. *J. Am. Chem. Soc.* **2006**, *128*, 1390–1393.
(268) Beattie, S. D.; Manolescu, D. M.; Blair, S. L. *J. Electrochem. Soc.* **2009**, *156*, A44–A47.
(269) Hardwick, L.; Freunberger, S.; Bao, J.; Paterson, A. J.; Bruce, P. G. In *IUPAC 2009*; Glasgow, Scotland Aug 2−7, 2009; Royal Society of Chemistry: London, 2009.
(270) Debart, A.; Paterson, A. J.; Bao, J.; Bruce, P. G. *Angew. Chem., Int. Ed.* **2008**, *47*, 4521–4524.
(271) Debart, A.; Bao, J.; Armstrong, G.; Bruce, P. G. *J. Power Sources* **2007**, *174*, 1177–1182.
(272) Wang, Y.; Zhou, H. J. Power Sources **2009**, in press.
(273) Visco, S. J.; Nimon, Y. S. U.S. Patent 2007/011707 A1, **2007**.